



CHORUS

This is the accepted manuscript made available via CHORUS. The article has been published as:

Colossal anisotropy of the magnetic properties of doped lithium nitrodometalates

V. P. Antropov and V. N. Antonov

Phys. Rev. B **90**, 094406 — Published 5 September 2014

DOI: [10.1103/PhysRevB.90.094406](https://doi.org/10.1103/PhysRevB.90.094406)

The nature of giant anisotropy of magnetic properties of doped lithium nitridometalates

V.P. Antropov¹ and V.N. Antonov^{1,2}

¹ Ames Laboratory USDOE, Ames, IA 50011

²Institute of Metal Physics, 36 Vernadsky Street, 03142 Kiev, Ukraine

(Dated: August 20, 2014)

We present the first principles investigation of the electronic structure and physical properties of doped lithium nitridometalates $\text{Li}_2(\text{Li}_{1-x}\text{M}_x)\text{N}$ (LiMN) with $\text{M} = \text{Cr}, \text{Mn}, \text{Fe}, \text{Co},$ and Ni . The diverse properties include the equilibrium magnetic moments, magneto-crystalline anisotropy, magneto-optical Kerr spectra and x-ray magnetic circular dichroism. We explain the huge magnetic anisotropy in LiFeN by its unique electronic structure which ultimately leads to a series of unusual physical properties. The most unique property is a complete suppression of relativistic effects and freezing of orbital moments for in-plane orientation of the magnetization. This leads to a huge spatial anisotropy of many magnetic properties including energy, Kerr and dichroism effects. LiFeN is identified as an ultimate single-ion anisotropy system where a nearly insulating state can be produced by a spin orbital coupling alone. A very non-trivial strongly fluctuating and sign changing character of the magnetic anisotropy with electronic doping is predicted theoretically. A very anisotropic and large Kerr effect due to the interband transitions between atomic like Fe 3d bands is found for LiFeN. A very strong anisotropy of the X-ray magnetic circular dichroism for the Fe K spectrum and a very weak one for the Fe $L_{2,3}$ spectra in LiFeN is also predicted.

PACS numbers: 75.50.Cc, 71.20.Lp, 71.15.Rf

I. INTRODUCTION

Lithium nitride, Li_3N , and ternary lithium nitridometalates $\text{Li}_2(\text{Li}_{1-x}\text{M}_x)\text{N}$ (LiMN), where M is a transition metal, have attracted considerable attention. They have emerged as promising candidates for anode materials,¹⁻³ electrolyte in Li-based batteries,⁴⁻⁶ and hydrogen storage mediums.⁷⁻⁹ In particular, LiMN ($\text{M} = \text{Fe}, \text{Co}$) has attracted much attention from battery engineers because of its large reversible capacity with a function of lithium source.¹⁰ Lithium nitride, Li_3N , is the only known thermodynamically stable alkali metal nitride. Li_3N forms two groups of ternary nitride compounds, one with the anti-fluorite structure and the other with the layered hexagonal, $\alpha\text{-Li}_3\text{N}$, a structure with four ions per unit cell at ambient conditions.^{11,12} Ternary lithium nitridometalates phases with $\text{M} = \text{Cu}, \text{Ni}, \text{Co}$ have already been reported as early as 1949 by Sachsze and Juza.¹³ Recently, the respective substitution phases with $\text{M} = \text{Mn}$ and Fe also were reported.^{14,15}

The electronic band structure of Li_3N and ternary lithium nitridometalates $\text{Li}_2(\text{Li}_{1-x}\text{M}_x)\text{N}$ have been calculated by several authors.¹⁶⁻²⁵ The lattice dynamic properties of Li_3N have been investigated using inelastic neutron scattering,²⁶ infrared Raman spectroscopy,²⁷ and *ab initio* calculations.^{22,23,28} The phonon dispersion curves of Li_3N have been studied by Kress²⁶ and Zhao.²⁹

The chemical and magnetic properties of the nitridometalate substitution series LiMN ($\text{M} = \text{Mn}, \text{Fe}, \text{Co}, \text{Ni}, \text{Cu}$) turned out to be very unusual.^{13,30} For the $\text{Mn}, \text{Fe}, \text{Co},$ and Ni compounds the +1 oxidation state of the 3d ion has been confirmed by x-ray absorption spectroscopy.³¹ Schnelle *et al.*³² investigated the electronic and magnetic properties of transition metal ni-

tridometalates LiMN ($\text{M} = \text{Co}, \text{Ni},$ and Cu). For the Ni series, for which the highest transition metal content could be achieved, the gradual insulator-metal transition was observed at $x \sim 0.8$ according to resistivity data. The samples of the other two series could be prepared with lower x and would show semiconducting behavior only. The effective magnetic moment per Ni-atom was found strongly exceed the spin-only value at low x . For higher x the magnetic moment decreases linearly towards zero.

Wu *et al.*^{24,25} studied the electronic structure and vacancy formation of Li_3N and LiMN ($\text{M} = \text{Co}, \text{Ni}, \text{Cu}$). They found that transition metal substitution significantly influence the electronic structures and the Li vacancy formation of Li_3N . The calculations indicate that transition metal substitution mainly takes place at Li(1) sites, which agree well with the experimental observations. Co or Ni substitutions can reduce the energy band gap and even change Li_3N from a semiconductor to a metallic-like conductor, which has the advantage of both electronic and ionic conduction. Transition metal substitution reduces the thermodynamic stability of Li_3N , which might benefit the intercalation and deintercalation of lithium during charge-discharge cycling in rechargeable lithium batteries.

Klatyk *et al.*¹⁹ have suggested that a rare interplay of crystal-electric-field effects and spin-orbit (SO) coupling causes a large orbital contribution to the magnetic moment of Fe in LiFeN. Based on a strong increase of the magnetization on cooling¹⁹ and on the Mössbauer spectroscopy^{19,33} a ferromagnetic ordering with $T \sim 65$ K was inferred for $x=0.21$, furthermore, huge hyperfine fields were found. The orbital contribution to the magnetic moment of Fe as well as the large hyperfine fields

were theoretically described within the framework of the local spin density approximation (LSDA).¹⁹ Novák and Wagner²⁰ calculated the electronic structure of LiMN ($x=0.17$ and $x=0.5$) using the supercell approach. They found that the splitting of two very narrow Fe energy bands at the Fermi level (E_F) due to SO coupling gave rise to a large orbital momentum, which was further enhanced by correlation effects. A giant uniaxial magnetocrystalline anisotropy was predicted. They also determined the electronic structures of related compounds with Co, Ni, and Cu instead of Fe.²¹ Furthermore, they discovered that these compounds correspond to a ferromagnetic insulator, a ferromagnetic half-metal and a nonmagnetic insulator, respectively.

Recently, Jesche *et al.*³⁴ successfully grew LiFeN single crystals with Fe concentrations ranging over three orders of magnitudes from $x=0.00028$ to 0.28. They showed that the LiFeN compound is insulating and that the N-Fe-N complex forms a linear molecule avoiding the Jahn-Teller distortion. They discovered a large coercivity in the LiFeN single crystal.

The aim of this work is the theoretical investigations of the electronic structures and physical properties of lithium nitridometalates LiMN, M = Cr, Mn, Fe, Co, and Ni. Section II of this paper presents the crystal structure of lithium nitridoferrates and computational details. Section III shows the results and discussions of obtained the electronic and magnetic structures, magnetic moments, the MO Kerr spectra, the X-ray magnetic circular dichroism and the magneto-crystalline anisotropy. These results are summarized in Section IV.

II. METHODOLOGY.

A. Cubic harmonics and SO interaction.

Cubic harmonics are very useful to describe the electronic structure of lithium nitridometalates. For $l=2$ cubic harmonics can be expressed in terms of real spherical harmonics \mathcal{Y}_{2m} as follows:

$$\begin{aligned} d_{3z^2-r^2} &\equiv \mathcal{Y}_{20} = Y_{20} \\ d_{yz} &\equiv \mathcal{Y}_{21}^{(-)} = i(Y_{2-1} + Y_{21})/\sqrt{2} \\ d_{xz} &\equiv \mathcal{Y}_{21}^{(+)} = (Y_{2-1} - Y_{21})/\sqrt{2} \\ d_{xy} &\equiv \mathcal{Y}_{22}^{(-)} = i(Y_{2-2} - Y_{22})/\sqrt{2} \\ d_{x^2-y^2} &\equiv \mathcal{Y}_{22}^{(+)} = (Y_{2-2} + Y_{22})/\sqrt{2} \end{aligned}$$

After a transformation of the coordinate system $z \rightarrow -x$:

$$\begin{aligned} d_{3z^2-r^2} &\rightarrow -\frac{1}{2}d_{3z^2-r^2} + \frac{\sqrt{3}}{2}d_{x^2-y^2} \\ d_{xz} &\rightarrow -d_{xz} \\ d_{yz} &\rightarrow d_{xy} \\ d_{x^2-y^2} &\rightarrow \frac{\sqrt{3}}{2}d_{3z^2-r^2} + \frac{1}{2}d_{x^2-y^2} \\ d_{xy} &\rightarrow -d_{yz} \end{aligned} \quad (1)$$

The SO interaction operator is defined by:

$$\hat{H}_{so} = c^{-2} \frac{2}{r} \frac{dV}{dr} (\hat{\mathbf{s}}) = \lambda (\hat{\mathbf{s}}) \quad (2)$$

where

$$\hat{\mathbf{s}} = \frac{1}{2} \begin{pmatrix} \hat{l}_z & \hat{l}_- \\ \hat{l}_+ & -\hat{l}_z \end{pmatrix} \quad (3)$$

$$\hat{l}_+ = \hat{l}_x + i\hat{l}_y; \quad \hat{l}_- = \hat{l}_x - i\hat{l}_y \quad (4)$$

Matrix elements of the \hat{l}_z operator are:

$$\begin{aligned} \hat{l}_z \mathcal{Y}_{l0} &= 0 \\ \hat{l}_z \mathcal{Y}_{lm}^{(-)} &= -\frac{im}{\sqrt{2}} [Y_{l-m} + (-1)^m Y_{lm}] = -im \mathcal{Y}_{lm}^{(+)} \\ \hat{l}_z \mathcal{Y}_{lm}^{(+)} &= -\frac{m}{\sqrt{2}} [Y_{l-m} - (-1)^m Y_{lm}] = im \mathcal{Y}_{lm}^{(-)} \end{aligned} \quad (5)$$

B. Magnetocrystalline anisotropy.

The internal energy of ferromagnetic materials depends on the direction of spontaneous magnetization. Here we consider one part of this energy, the magnetic anisotropy energy (MAE), which possesses the crystal symmetry of the material. For the material exhibiting uniaxial anisotropy, such as a hexagonal crystal, the MAE can be expressed as³⁵

$$\begin{aligned} K &= K_1 \sin^2 \theta + K_2 \sin^4 \theta + K'_3 \sin^6 \theta \\ &\quad + K_3 \sin^2 \theta \cos[6(\phi + \psi)] + \dots \end{aligned} \quad (6)$$

where K_i is the anisotropy constant of the i th order, θ is a polar angle and ϕ is a phase angle of the Cartesian coordinate system.

Here, we study the MAE and MO Kerr effect caused only by the SO interaction. The MAE is defined below as the difference between two self-consistently calculated relativistic total energies for two different magnetic field directions, $E(\theta) - E(0001)$. We also investigate the orbital moment anisotropy (OMA) defined as the difference between two self-consistently calculated orbital magnetic

moments M_l for two different magnetic field directions, $M_l(0001) - M_l(\theta)$.

As we show below the doped lithium nitridometalates represent a good example where the MAE and OMA have close relations. This is usually shown by adding the spin orbital coupling and using the second order perturbation theory (PT). Such correction was first widely discussed and used in different construction of the spin Hamiltonian.³⁶ In the seminal paper by Yosida, Okiji and Chikazumi³⁷ using impurity Green function approach several relations between different spin contributions to MAE and OM have been obtained. Many years later this approach with different approximations was widely used in different areas.³⁸⁻⁴² A generalization of single impurity approach was presented in Ref. 43. Most recent reviews with different applications can be found in Ref. 44,45. Below we will mostly use the original single impurity approach³⁷ because it is ideally suited for our single-site anisotropy system (see below). In considered PT formalism the SO energy by definition (Eq. 3) is^{37,38}

$$E_{so} = -\frac{\lambda}{2} \left(L_z^{\uparrow\uparrow} + L_z^{\downarrow\downarrow} + L_+^{\uparrow\downarrow} + L_-^{\downarrow\uparrow} \right), \quad (7)$$

where $L_i^{\sigma\sigma'}$ is the matrix element of the i -component of the orbital moment \hat{l}_i between corresponding spin states. The total relativistic energy of the system is a sum of the SO energy and a corresponding relativistic response of kinetic and potential energies. In general quantum mechanical PT it has been shown⁴² that the second order correction to the total energy change is just a half of the first order of the total energy of a perturbation term. Thus in this order the system response above is always negative and leads to the effective screening of initial SO energy by half. Correspondingly a total relativistic energy of the system is a simple scaling of the SO energy

$$E = E_{so}/2 \quad (8)$$

or for the total relativistic energy change

$$E = -\frac{\lambda}{4} \left(L_z^{\uparrow\uparrow} + L_z^{\downarrow\downarrow} + L_+^{\uparrow\downarrow} + L_-^{\downarrow\uparrow} \right). \quad (9)$$

A total orbital moment is defined as

$$M_l = M_l^{\uparrow\uparrow} + M_l^{\downarrow\downarrow} = -L_z^{\uparrow\uparrow} + L_z^{\downarrow\downarrow}, \quad (10)$$

The negative sign for spin up component appears explicitly only when PT is used, while in fully relativistic Dirac approach all spin components formally have the same sign. For spin longitudinal components of the total energy one can write

$$E^{\sigma\sigma} = \sigma_z \frac{\lambda}{4} M_l^{\sigma\sigma}, \quad (11)$$

where $\sigma_z = 1(-1)$ for $\sigma = \uparrow(\downarrow)$.

This ratio simply emphasizes that a minimum of the total energy for each spin component corresponds to a larger orbital moment for the same component (which is just a Hund's rule statement for each spin component). While it is valid for each spin component separately there is clearly no such relation between the total energy and the total orbital moment due to a presence of the negative sign in Eq. 9 for spin up component.

The expressions of Eqs. 9 and 11 are obtained under following assumptions. First, the SO parameter is much smaller than crystal fields, spin splittings and the effective width of bands contributing to the SO coupling. Those are requirements of the traditional Rayleigh-Schrodinger PT for non-degenerate levels. In addition, PT requires the potential to be 'frozen' and Fermi level unchanged. It is not evident that the modern addition of the SO coupling to the scalar relativistic Hamiltonians with their diagonalization, proper treatment of energy dependence of the SO coupling and consecutive self-consistent procedure would allow this simple relation to be fulfilled. Not only such treatment corresponds to PT for the degenerate levels, the additional self-consistency effects and Fermi level modifications can dramatically change the PT conclusions.

However, the recent calculations of this relation in many metals with a very different strength of the SO coupling show⁴² that this expression is still fulfilled in realistic systems with a possible error of just 5-10% in most of the considered systems. As a result, it seems that this approach as a whole is justified for the analysis of relativistic energies on a scale of the typical SO coupling energies (0.05 – 1 eV).

A situation becomes worse when the effects of the MAE (0.01 – 20 meV) are analyzed using this approach. All errors from the different levels of PT contribute to the total uncertainty making the whole technique less reliable. However, qualitatively many relations are still hold as we can see for considered below doped LiFeN systems. Let us now consider these effects in details. The MAE in this approximation can be presented as

$$K = \frac{\lambda}{4} \left(\Delta L_z^{\uparrow\uparrow} + \Delta L_z^{\downarrow\downarrow} + \Delta L_+^{\uparrow\downarrow} + \Delta L_-^{\downarrow\uparrow} \right) \\ = K^{\uparrow\uparrow} + K^{\downarrow\downarrow} + K^{\uparrow\downarrow} + K^{\downarrow\uparrow}, \quad (12)$$

where $\Delta L_z^{\uparrow\uparrow}$ corresponds to the difference of orbital moments with magnetic field along z and x directions thus representing a spin up component of the OMA, which is written as

$$\Delta M_l = -\Delta L_z^{\uparrow\uparrow} + \Delta L_z^{\downarrow\downarrow}, \quad (13)$$

Thus, a simple relation between different spin longitudinal components of the MAE and the OMA holds

$$K^{\sigma\sigma} = -\sigma_z \frac{\lambda}{4} \Delta L_z^{\sigma\sigma}, \quad (14)$$

emphasizing that an easy magnetization axes direction for each spin component separately corresponds to a larger orbital moment for the same spin component (which is also just a Hund's rule statement for each spin component). While it is valid for each spin component separately there is no such relation between the total MAE and the total OMA due to a presence of the negative sign in Eq. 13 for spin up component.^{44,45} Let us now consider a case of a half metallic system with only spin down states at and near E_F , so no spin-flip transitions can be excited by the SO coupling. In this case the L_z moments for out of plane and in-plane directions of magnetization became:³⁷⁻⁴¹

$$L_{\parallel}^{\sigma\sigma} = \frac{\lambda}{\pi} \int^{\varepsilon_F} d\varepsilon \text{Im} (4G_{xy}^{\sigma} G_{x^2-y^2}^{\sigma} + G_{xz}^{\sigma} G_{yz}^{\sigma}) \quad (15)$$

and

$$L_{\perp}^{\sigma\sigma} = \frac{\lambda}{\pi} \int^{\varepsilon_F} d\varepsilon \text{Im} [(3G_{3z^2-r^2}^{\sigma} + G_{x^2-y^2}^{\sigma} + G_{xy}^{\sigma}) G_{yz}^{\sigma}] \quad (16)$$

where G_{xz}^{σ} is the element of a non-relativistic Green function for spin σ and xz symmetry.^{37,41-43} This structure of non-zero elements of the relativistic coupling between different cubic harmonics can be seen directly from Tab.I and II below. In addition, the on-site Green function can have off-diagonal elements even for d-electrons (for instance, for hexagonal symmetry). These elements have not been taken into account in the above expressions (see Ref. 43 for more details).

Now, if the only to cross E_F are xy and $x^2 - y^2$ spin down states and all other d -states are situated far from the E_F , then

$$L_{\parallel}^{\sigma\sigma} = \frac{\lambda}{\pi} \int^{\varepsilon_F} d\varepsilon \text{Im} (4G_{xy}^{\sigma} G_{x^2-y^2}^{\sigma}) \quad (17)$$

while in plane all relativistic couplings disappear (our model does not have anymore any states supporting such couplings in plane) and $L_{\perp}^{\sigma\sigma} = 0$.

The total MAE in this case coincides with the total relativistic energy of spin down states and can be presented as³⁷⁻⁴²

$$K = K^{\downarrow\downarrow} = \frac{\lambda}{4} L_z^{\downarrow\downarrow} = \frac{m^2}{4} \lambda^2 N_m^{\downarrow}(E_F) \quad (18)$$

Clearly the PT relation for the orbital moment $L^{\downarrow\downarrow} = \lambda m^2 N_m^{\downarrow}$ will be strongly violated in the case of a very narrow peak when the value of $L^{\downarrow\downarrow}$ will be unphysically large. In addition, such simplified expression cannot describe anisotropy of M_l . Also in this case while λ for 3d atoms is much smaller than the crystal field splittings, it can be comparable with the bandwidths of xy and $x^2 - y^2$ narrow peaks at the E_f and PT is no longer valid. The real typical example will be an atom ($N_m^{\downarrow} \rightarrow \infty$) where

$L^{\downarrow\downarrow}$ has limited and integer values of 0,1,2,... To obtain a proper description of the orbital moment in the atomic limit one has to go beyond the second order of traditional Rayleigh-Schrodinger PT. Alternatively one can use the Brillouin-Wigner PT⁴⁶ which allows to resolve this issue already in the second order. In this approach the relativistic modification of the DOS N_m^{\downarrow} will be $N/\sqrt{1+m^2\lambda^2N^2}$, so the orbital moment for the spin down component is written as

$$L^{\downarrow\downarrow} = m \frac{m\lambda N_m^{\downarrow}}{\sqrt{1+(m\lambda N_m^{\downarrow})^2}}, \quad (19)$$

and in the atomic limit

$$L^{\downarrow\downarrow} = \lim_{N_m^{\downarrow} \rightarrow \infty} \left(m \frac{m\lambda N_m^{\downarrow}}{\sqrt{1+(m\lambda N_m^{\downarrow})^2}} \right) = m, \quad (20)$$

and for considered above degenerate $x^2 - y^2$ and xy orbitals at the E_f it will be equal 2 for any value of the SO parameter λ , while for specific non-relativistic case of $\lambda = 0$ $L^{\downarrow\downarrow} = 0$. Thus the account of a proper relativistic modification of the effective band width in the case of nearly atomic d-systems or f-systems with large DOS at the E_f ⁴⁷ is crucial for the correct description of both the orbital moment and its anisotropy. The second order of the usual Rayleigh-Schrodinger PT does not describe the orbital moment or its anisotropy correctly.

Typically the atomic SO constant in 3d atoms is around $\lambda=0.05$ eV therefore for the orbital moment $M_l=2$ one can expect that the theoretical maximum of MAE can reach 25 meV. Let us summarize all conditions of our model. All spin up states should be far from the E_f . It corresponds to the effective spin splitting being much larger than a characteristic SO energy. A spin splitting of 1 eV would be already sufficient. Next, crystal field splitting separating states at E_f and all other d-states with the same spin should be at least as large as the exchange splitting. We will show below that LiFeN system satisfies all those requirements with the resulting MAE being very close to our simple estimation above.

C. Structural model.

Li₃N crystallizes in a layered hexagonal structure, α -Li₃N, with four ions per unit cell at ambient conditions. The unit-cell dimensions are $a = 3.648$ Å and $c = 3.875$ Å^{4,48} with the symmetry point group of $D6h$ (space group $P6/mmm$) with two different lithium sites, Li(1) and Li(2). Li(1) ions occupy the 1b Wyckoff positions ($x = 0, y = 0, z = \frac{1}{2}$), Li(2) ions occupy the 2c positions ($x = \frac{1}{3}, y = \frac{2}{3}, z = 0$), N ions are in the 1a positions ($x = 0, y = 0, z = 0$). The Li₂N layer is formed by Li(2)

in the ab plane with edge-shared N-Li₆ hexagons and Li(1) positions between layers to form continuous Li(1)-N-Li(1) chains along the c -axis (Fig. 1, upper panel). The N atoms have 8 Li atoms as nearest neighbors: two at 1.9375 Å distance along the c axis and six Li at 2.1062 Å in ab plane. Earlier X-ray diffraction and powder neutron diffraction studies reported 1-2% vacancies in Li(2) position at room temperature.⁴⁹ The vacancy concentration can go up to 4% at high temperatures.

As indicated by the notation of the chemical formula, the substituted metal ions M occupy only the Li(1) 1b Wyckoff position, which is sandwiched between the Li(2)₂N layers. Therefore, the structure of lithium nitridoferrates Li₂(Li_{1-x}M_x)N consists of alternating (Li₂N) and (Li_{1-x}M_x) planes that are perpendicular to the hexagonal c axis (Fig. 1). Fe substitution causes an increase of a , but a decrease of c by 1.1% and 1.5%, respectively, for $x=0.28$ with intermediate concentrations showing a linear dependence on x following Vegard's law.³⁴ Along the chains parallel to the c -axis the cations alternate as -N-Fe-N-Li-N-Fe-. Iron is strongly bonded to the two nitrogen ions lying in the chain parallel to the c -axis. Its bonding in the (Li_{1-x}Fe_x) plane is weak and it depends on the relative number of Li and Fe neighbors in the plane.

Analysis of the Mössbauer spectra¹⁹ indicates that the distribution of M ions in the (Li_{1-x}M_x) planes is random. There are some indications for preferred configurations within the lateral Li,M-plane (depending on preparation temperature, cooling rate, transition metal M and composition parameter x), but no superstructure based on crystallographic data could be presented so far.³¹ We neglected the disorder effect in the (Li_{1-x}Me_x) planes and used the supercell method to calculate the electronic structure and physical properties of the lithium transition metal nitridometalates. Similar approximation was also used in previous publications.¹⁹⁻²¹

D. Calculation details.

The calculations presented in this work were performed using the spin-polarized fully relativistic LMTO method⁵⁰. To understand the influence of the SO interaction on the MO properties and MAE we also used the scalar relativistic magnetic Hamiltonian with the SO coupling added variationally.⁵¹

The electronic structure and physical properties of lithium transition metal nitridometalates LiMN (M = Cr, Mn, Fe, Co, and Ni) calculated using the super-cell approximation for $x= 0.083, 0.167, 0.333$ and 0.5 . The $x=0.167$ and 0.5 corresponds to the *hex1* and *hex2* structures, respectively, in notation of Ref. 20. The basis consisted of s , p , d , and f LMTO's at the transition metal sites and s , p , and d LMTO's at the Li and N sites. The \mathbf{k} -space integration were performed with the improved tetrahedron method.⁵² To attain good convergence in total energy a large number of \mathbf{k} points has to be

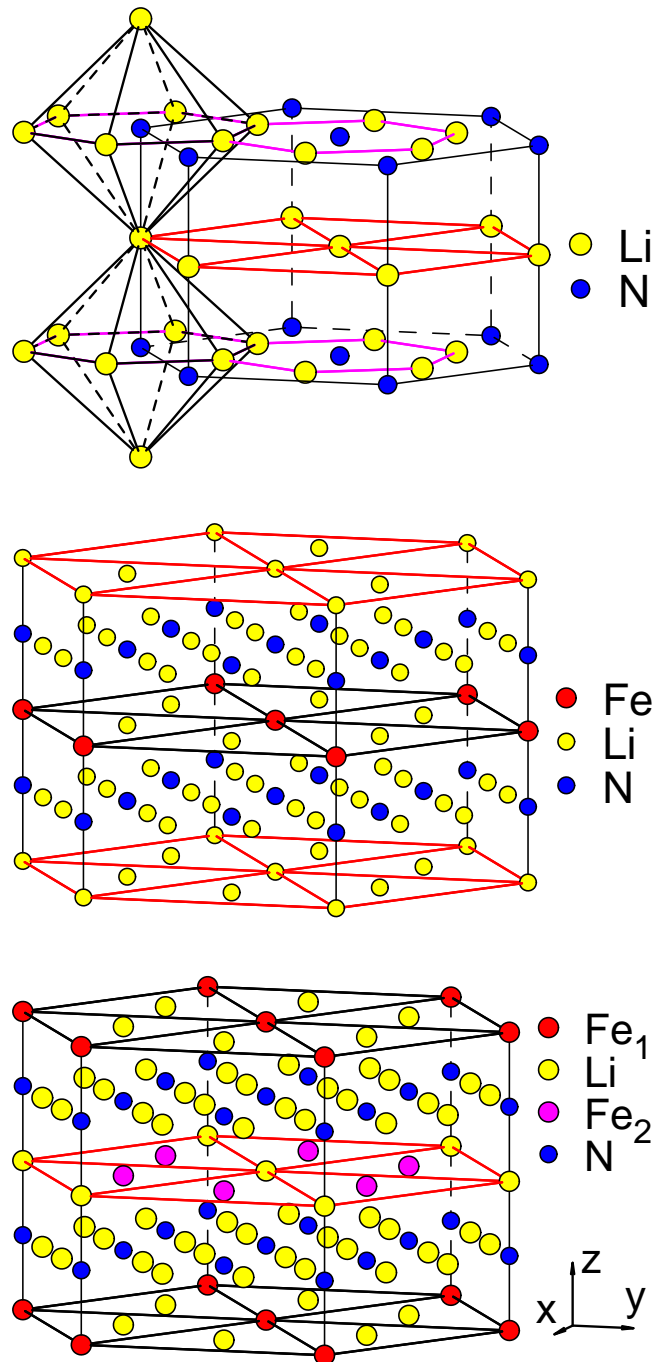


FIG. 1: (Color online) Crystal lattice of α -Li₃N (upper panel), Li₂(Li_{1-x}Fe_x)N for $x=0.17$ (middle panel) and Li₂(Li_{1-x}Fe_x)N for $x=0.5$ (lower panel).

used in the calculations. To resolve the difference in total energies and to investigate the convergence we used 1200 and 2413 \mathbf{k} points in the irreducible part of the Brillouin zone, which corresponds to 21952 and 46652 \mathbf{k} points in full zone.

We used the "relativistic" generalization of the LSDA+ U method⁵³ which takes into account the SO

coupling so that the occupation matrix of localized electrons becomes non-diagonal in spin indexes. A double-counting correction term was used in the fully-localized limit approximation.^{54,55} We used $U = 0.89, 2, 3,$ and 4 eV with $J = 0.89$ eV for the transition metal sites. In this case $U = 0.89$ eV $U_{\text{eff}} = U - J = 0$ and the effect of the LSDA+ U comes from non-spherical terms which are determined by F^2 and F^4 Slater integrals.⁵³ Such the approximations denoted as orbital polarization (OP) correction in what follows is similar to the traditional OP approach⁵⁶ but has no adjusted parameters.

III. ELECTRONIC STRUCTURE OF LiFeN.

A. Energy band structure.

Figure 2 presents partial densities of states of LiFeN for $x=0.17$ calculated within LSDA. The results are in good agreement with previous studies.^{19–21} N $2s$ states situated at the -13.7 to -12.3 eV below E_F . N $2p$ states occupy the -5.5 to 11.5 eV energy range and strongly hybridize with Mn $3d$ states in the -4 to 3 eV energy range. Li $2p$ states occupy the similar interval as N $2p$ ones. The spin splitting of Li and N $2p$ states is quite small. The crystal field at the Fe site (D_{6h} point symmetry) causes the splitting of d -orbitals into a singlet a_{1g} (d_{3z^2-1}) and two doublets e_{1g} (d_{xz} and d_{yz}) and e_{2g} (d_{xy} and $d_{x^2-y^2}$). We found that the ground state for LiFeN is a ferromagnetic state with estimated Curie temperature about 120 K. This estimation has been done by using the obtained total energy difference between ferro and anti-ferromagnetic states with consecutive usage of the mean field expression for the localized Heisenberg-spin model.

Matrix elements of l_z and $l_{+/-}$ between the cubic harmonics are collected in Table I and II, respectively.

For the expected Fe $3d^6$ configuration the majority spin electrons occupy all five orbital states, while the distribution of the minority spin electrons depends on the energy sequence of a_{1g} , e_{1g} and e_{2g} states. Fe d_{xy}^\downarrow and $d_{x^2-y^2}^\downarrow$ (e_{2g}) are the states which lie in the plane perpendicular to Fe-N bonds and, thus, do not hybridize with N p states. As a result they have the lowest energy. Fe d_{zx}^\downarrow and d_{yz}^\downarrow (e_{1g}) form $pd\pi$ bonds with N p_x and p_y and are shifted to higher energy while $d_{3z^2-1}^\downarrow$ forms an extremely strong $pd\sigma$ bond and lies even higher.

In spin-polarized calculations d_{xy}^\downarrow and $d_{x^2-y^2}^\downarrow$ bands are filled by one electron. The width of these bands is extremely small as they lie in a gap of Li and N states and direct Fe-Fe hybridization is very weak. It turns out that the width is comparable to the SO interaction strength. Figure 3 presents the energy band structure of LiFeN using a non-relativistic approximation (a), as well as fully relativistic with $\mathbf{M} \parallel c$ (b) and \mathbf{M} in the ab plane (c). Fig. 5 presents total DOS calculated in the fully relativistic approximation with $\mathbf{M} \parallel c$ (upper panel) and $\mathbf{M} \perp c$ axes (lower panel). The relativistic

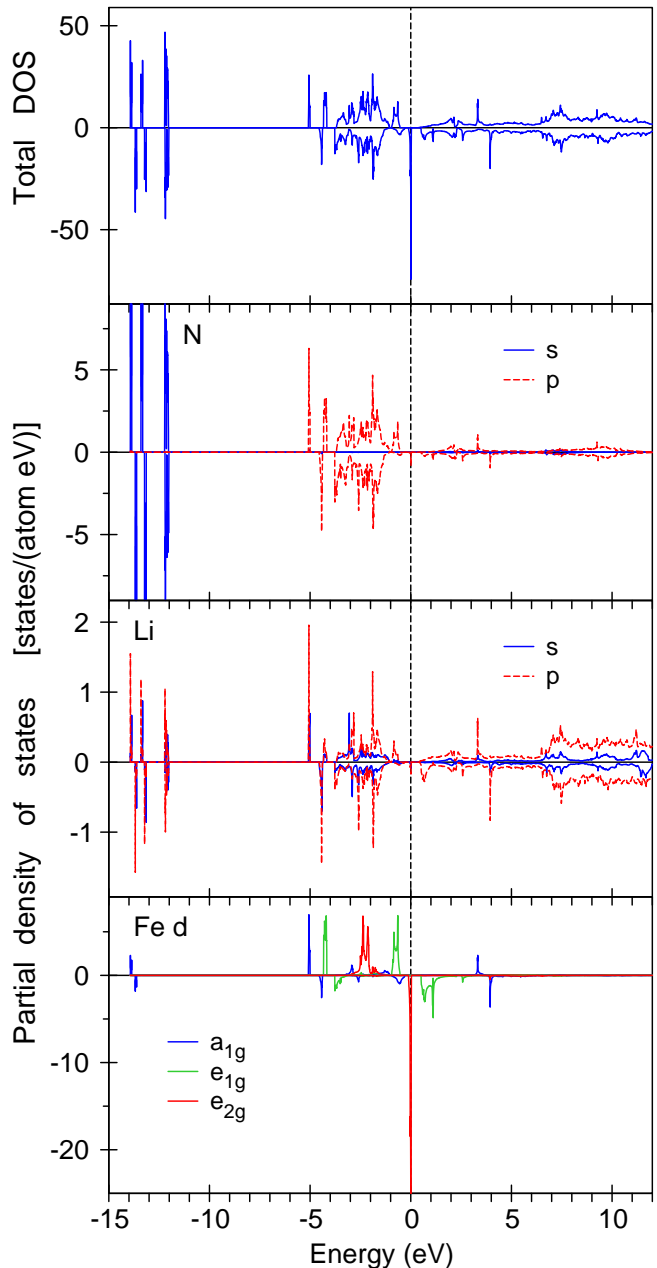


FIG. 2: (Color online) The LSDA total [in states/(cell eV)] and partial densities of states of LiFeN for $x=0.17$.

effects create a nearly insulated state for $\mathbf{M} \parallel c$. Thus, this system cannot be considered as Mott-Hubbard or Slater types insulators and can be called a SO coupling generated insulator.

Because of the large spin splitting of Fe $3d$ states spin-flip terms of the SO interaction are suppressed. Table I shows that the only non-zero matrix elements of l_z are $\langle d_{xz} | l_z | d_{yz} \rangle$ and $\langle d_{xy} | l_z | d_{x^2-y^2} \rangle$. All other diagonal elements are equal to zero. Therefore when $\mathbf{M} \parallel c$, the diagonal $\hat{s}\mathbf{l}$ term couples d_{xy} and $d_{x^2-y^2}$ so the e_{2g} states are split due to the SO interaction and form states with

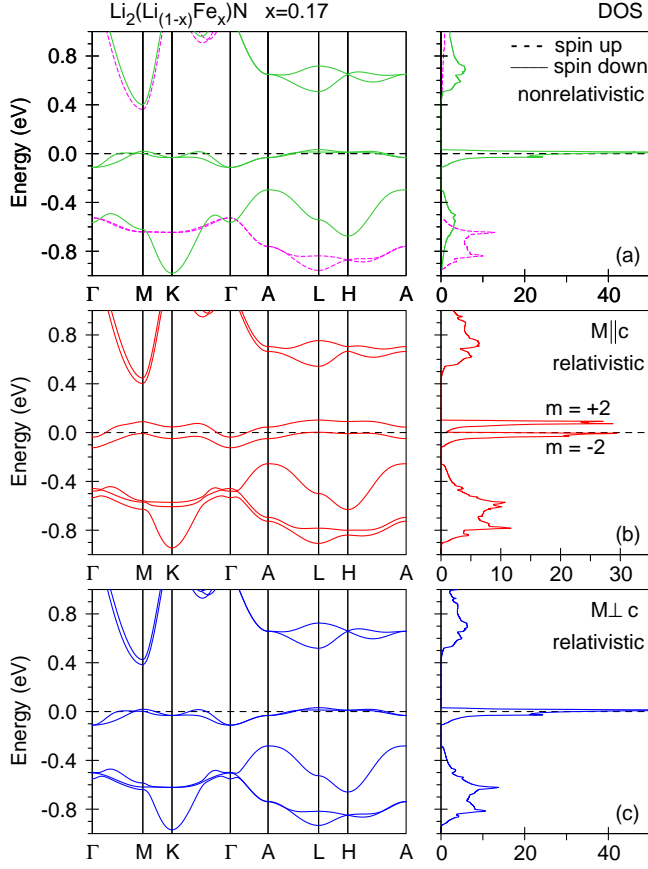


FIG. 3: (Color online) Energy band structure and DOS [in states/(cell eV)] of LiFeN for $x=0.17$: a non-relativistic (a), fully relativistic $\mathbf{M} \parallel c$ (b), and $\mathbf{M} \perp c$ (c).

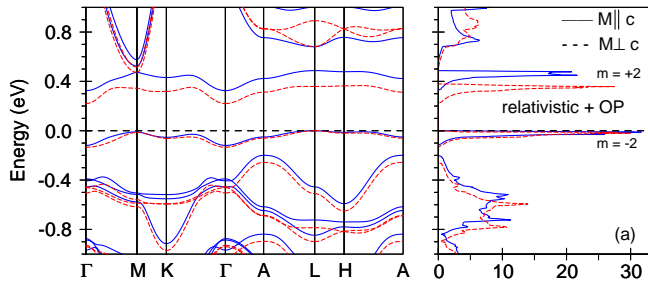


FIG. 4: (Color online) Energy band structure and DOS [in states/(cell eV)] of LiFeN for $x=0.17$ in fully relativistic approximation with orbital polarization correction with $\mathbf{M} \parallel c$ (full blue lines) and $\mathbf{M} \perp c$ (dashed red lines), correspondingly.

$m = -2$ and $m = +2$. Because of the small band width of the e_{2g} states, the band formed by the $m = -2$ state is almost completely filled and the $m=2$ band is almost completely empty (Fig. 3(b) and Fig. 5 upper panel). This gives the huge value of M_l of $1.477 \mu_B$ which is almost completely quenched in this case. This situation

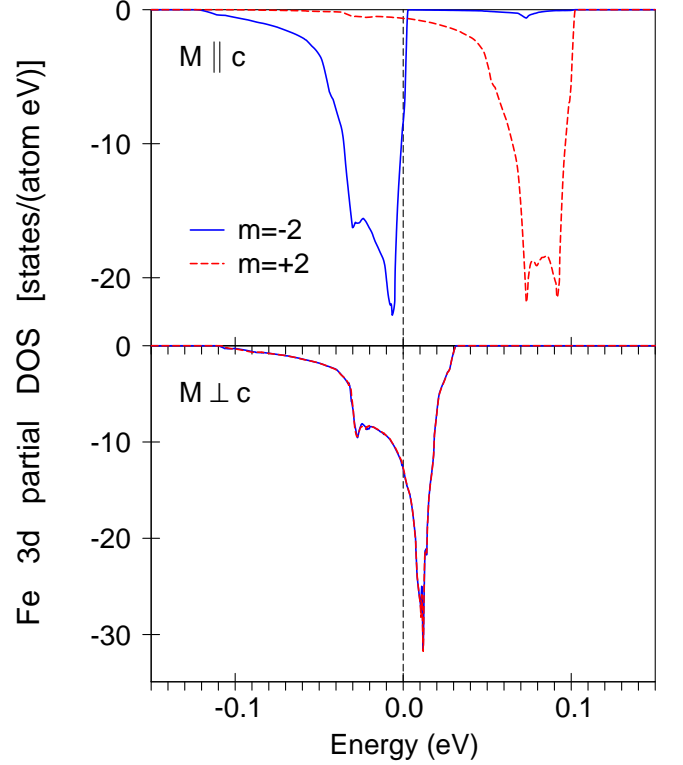


FIG. 5: (Color online) Fe 3d partial DOS of LiFeN for $x=0.17$ in close vicinity of E_F calculated in the fully relativistic approximation with $\mathbf{M} \parallel c$ (upper panel) and $\mathbf{M} \perp c$ (lower panel).

is very rare because it is usually accepted that a crystal field quenches a part or all of the orbital momentum of a free ion in 3d metals. When $\mathbf{M} \perp c$, in the local frame with $z' \parallel \mathbf{M}$ the d_{xy} and $d_{x^2-y^2}$ orbitals are transformed into other orbitals (e.g. $d_{xy} \rightarrow d_{yz}$, $d_{x^2-y^2} \rightarrow$ linear combination of $d_{x^2-y^2}$ and d_{3z^2-1} , see Eqs. 2), so the diagonal SO matrix elements between these orbitals are equal to zero (Table I). Since the spin-flip SO interaction terms are still suppressed by large spin-splitting M_l becomes almost quenched ($M_l^\perp = 0.063 \mu_B$) while the total energy increases as compared to $E_{M \parallel c}$. The only non-zero contributions from the SO interaction come from the off-diagonal in spin $l_{+/-}$ terms. As a result, the energy bands for a non-relativistic (Fig. 3 (a)) and fully relativistic ($\mathbf{M} \perp c$) (Fig. 3 (c)) are very similar. The corresponding peak in the DOS is not split due to SO interaction (Fig. 5 lower panel). This result is illustrated also by Eqs. 15-8 where the situation with $x^2 - y^2$ and xy orbitals for the spin down is described using orbital moment calculations in perturbation theory.

Jesche *et al.*³⁴ recently demonstrated that the LiFeN compounds are insulators for x varying from 0.00028 to 0.28, however, they did not estimate the value of the energy gap. The LSDA+SO calculations produce a quasi-gap at E_F for $\mathbf{M} \parallel c$ (Fig. 5 upper panel) and a metallic state for $\mathbf{M} \perp c$ (Fig. 5 lower panel). Thus, not only

TABLE I: Matrix elements of $\langle \mathcal{Y}_{2m} | l_z | \mathcal{Y}_{2m} \rangle$ between the d cubic harmonics.

	d_{yz}	d_{xy}	d_{xz}	d_{3z^2-1}	$d_{x^2-y^2}$
d_{yz}	0	0	i	0	0
d_{xy}	0	0	0	0	$2i$
d_{xz}	$-i$	0	0	0	0
d_{3z^2-1}	0	0	0	0	0
$d_{x^2-y^2}$	0	$-2i$	0	0	0

TABLE II: Matrix elements of $\pm \langle \mathcal{Y}_{2m} | l_{\mp} | \mathcal{Y}_{2m} \rangle$ between the d cubic harmonics.

	d_{yz}	d_{xy}	d_{xz}	d_{3z^2-1}	$d_{x^2-y^2}$
d_{yz}	0	∓ 1	0	$-i\sqrt{3}$	$-i$
d_{xy}	± 1	0	$-i$	0	0
d_{xz}	0	i	$\pm\sqrt{3}$	∓ 1	0
d_{3z^2-1}	$i\sqrt{3}$	0	$\mp\sqrt{3}$	0	0
$d_{x^2-y^2}$	i	0	± 1	0	0

the insulating state can be obtained by the SO coupling addition, such metal-insulator transition can be tuned by a rotation of the magnetization of the ferromagnetic state. While relativistic insulators are known, we are not familiar with other examples of metallic systems where the metal-insulator transition appears as a result of magnetization rotation. This effect is rather unusual and has to be verified experimentally.

We also calculated the energy band structure of LiFeN using the LSDA+ U method for $U=0.89, 2, 3,$ and 4 eV with $J=0.89$ eV. We found that already the OP correction ($U_{\text{eff}} = U - J = 0$) produces an insulating solution both for the $\mathbf{M} \parallel c$ and $\mathbf{M} \perp c$ (Fig. 4) in agreement with the experiment.³⁴ All the explanations about the MAE in this compound presented above for the LSDA approach are valid also for the LSDA+OP approach. The energy band formed by the $m = -2$ state is completely filled and the $m=+2$ band is completely empty. The M_l which is unquenched and equal to $1.623 \mu_B$ for $\mathbf{M} \parallel c$ is larger than the LSDA result. The orbital moment is almost quenched for $\mathbf{M} \perp c$ ($M_l^\perp = 0.069 \mu_B$). The energy position of the empty $m=+2$ state for the $\mathbf{M} \parallel c$ is shifted upward by the SO splitting in comparison with the similar band for the $\mathbf{M} \perp c$ state.

For the LSDA+ U calculations with $U=2, 3,$ and 4 eV the energy bands formed by the $m = -2$ and the $m=+2$ states are shifted downward and upward, respectively, progressively with increasing Hubbard parameter U (not shown). The M_l are also increased, for $\mathbf{M} \parallel c$ and they became equal to $1.656, 1.662,$ and $1.651 \mu_B$ for $U = 2, 3,$ and 4 eV, respectively.

Fig. 6 shows the MAE (lower panel) and M_l as a function of the magnetization direction in LiFeN for $x=0.08, 0.17, 0.33,$ and 0.5 calculated in the LSDA. There is a huge MAE ($E_{M\parallel c} - E_{M\perp c}$) equal to -32.2 and -29.2

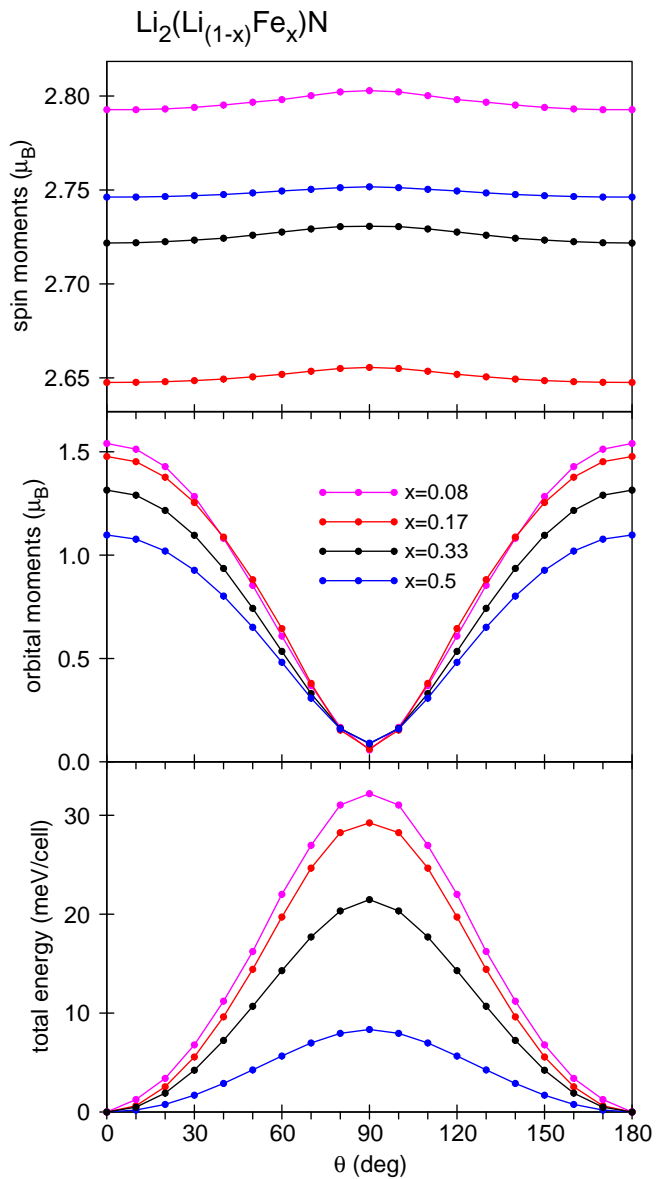


FIG. 6: (Color online) The total energy (lower panel), M_s (upper panel) and M_l (middle panel) as a function of the magnetization direction in LiFeN for $x=0.08, 0.17, 0.33,$ and 0.5 calculated in the LSDA.

meV in lithium nitridoferrates for $x=0.08$ and $0.17,$ respectively. However, MAE is rapidly decreased with an increase of Fe concentration and becomes relatively small namely -8.3 meV for $x=0.5$. Our results slightly differ from the previously published data of Nowak and Wagner.²⁰ They obtained the MAE equal to -10.5 and -24.0 meV for $x=0.5$ and $0.17,$ respectively. Some differences can be explained by the usage of different band structure methods (fully relativistic Dirac spin-polarized LMTO here and LAPW with the SO coupling treated as perturbation in Ref. 20). We also used a different LSDA+ U scheme.

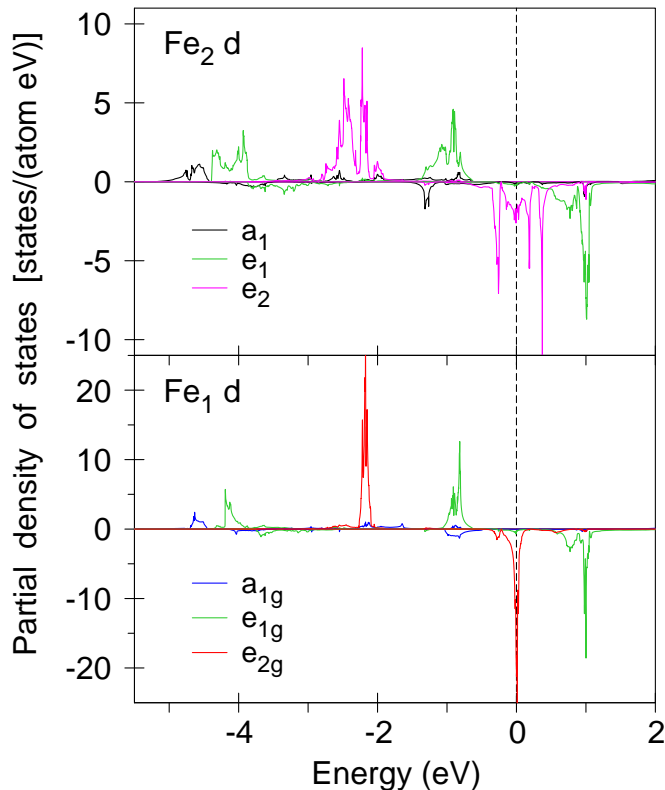


FIG. 7: (Color online) The LSDA partial densities of states of LiFeN for $x=0.5$.

Figure 7 presents the LSDA partial densities of states of LiFeN for $x=0.5$. The Fe₁ ion still has very narrow bands at E_F of e_{2g} symmetry, which produces a quite large orbital magnetic moment at the Fe₁ site of $1.098 \mu_B$ for $\mathbf{M} \parallel c$. The Fe₁ ions have six Li neighbors, while ions Fe₂ have three Fe and three Li neighbors in the Li_{1-x}Fe_x plane. Therefore, due to Fe₂–Fe₂ hybridization the Fe₂ e_2 (d_{xy} , $d_{x^2-y^2}$) bands are much broader. As a consequence, the SO coupling produces a much smaller orbital moment ($M_l^{\parallel} = 0.322 \mu_B$). In our calculations we used the super-cell approximation with fixed positions of Fe₁ and Fe₂ ions. In real systems the distribution of Fe ions in the Li_{1-x}Fe_x planes is random,¹⁹ therefore one would expect the M_l being averaged between M_l of these two positions.

To investigate the influence of Fe₁ and Fe₂ atoms on the MAE we calculate self-consistently the MAE independently switching off the SO interaction on the Fe₁ and Fe₂ sites. If we set the SO coupling on the Fe₁ (Fe₂) site to zero the MAE reduces to -2.1 (-6.1) meV. The MAE in LiMnN ($x=0.5$) was found as large as -8.3 meV. Therefore, LiFeN presents quite a rare example of the single-ion anisotropy d -compound where due to strong localization of the $3d$ orbital the pair Néel anisotropy is very small. Such a situation is more typical for the rare-earth compounds where the $4f$ states usually are strongly localized.

We also investigated the MAE for other lithium nitridometalates LiMN ($M = \text{Cr, Mn, Co, and Ni}$). Fig. 8 shows the MAE (lower panel) and M_l as a function of the magnetization direction in LiMN ($M = \text{Cr, Mn, Co, and Ni}$) for $x=0.17$ calculated in the LSDA. The corresponding transition metal $3d$ partial densities of states present in Fig. 11. The MAE for these systems are at least one order of magnitude smaller than the MAE for lithium nitridoferrate. Besides, only LiNiN has the same easy axis of magnetization as lithium nitridoferrate, namely, along c direction. The easy axes of magnetization for $M = \text{Cr, Mn, and Co}$ are in the ab plane. The M_l for these lithium nitridometalates are also significantly smaller than the moments in lithium nitridoferrate (compare upper panels of Figs. 6 and 8). The Cr M_l is opposite to the spin moment reflecting a behavior which is typical for a less than half filled d -band.

On Fig. 9 we show both MAE and OMA for all considered systems for $x=0.17$. While clearly $K \sim \Delta M_l$ for all systems, for Cr atoms there is opposite ratio and $K \sim -\Delta M_l$. This inverse proportionality is related also to the Hund's rule for a less than half filled d -band or larger DOS for spin up states around the E_f (see discussion in⁴²). However, coefficient proportionality is not simple $\lambda/4$ and its absolute value fluctuates from atom to atom. This disagreement most likely related to a peculiar very narrow peaks structure of DOS near the E_f . While a correct description of such narrow peaks requires high accuracy for a metallic state, the application of the second order Rayleigh-Schrodinger PT can be questioned. Fortunately, the self-consistent calculations with the SO coupling included as a second variation correspond to the PT for the degenerate levels and such approach produces reliable in this sense results. The self-consistency also contributes to the deviation from the analytical PT ratio $\lambda/4$ between the MAE and the OMA (Eq. 13).

We found that in our case (Fig.9) this coefficient of proportionality is close to $\lambda/2$ indicating that the SO coupling is no longer screened and the total MAE appears to be close to the magnetic anisotropy of the SO coupling alone $K = K_{so}$. This rather unusual result also can serve as an indicator of a strong violation of the second order PT.

To obtain anisotropy constants of different order we fit the obtained the angular dependencies of the total energy with the function from Eq. 6. The results for LiFeN are presented on Fig. 10 as a function of the Fe concentration. While K_1 constant is dominating for all concentrations, the K_2 and K_3 constants do not show any decrease with an order of the constant with K_3 being always somewhat larger and positive, while K_2 is a sign changing fluctuating with temperature quantity. One can relate such non-smooth behavior of K_n to the violation of PT applicability discussed above.

For the expected Mn $3d^5$ configuration the majority spin electrons occupy all five orbital states, while the minority spin electrons states are empty. The exchange splitting of the e_{2g} and e_{1g} states is increased by approx-

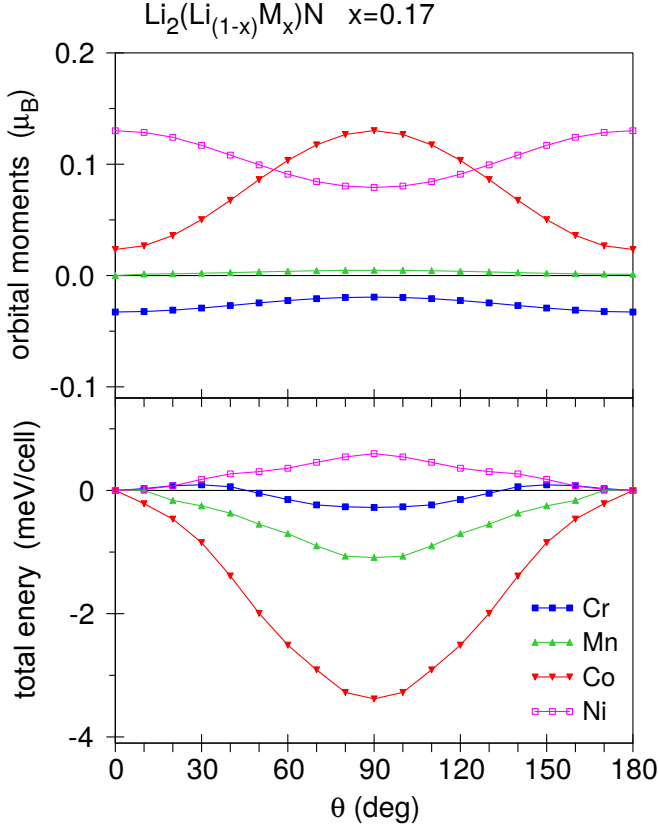


FIG. 8: (Color online) The total energy (lower panel) and M_l moments (upper panel) as a function of the magnetization direction in LiMnN $M = \text{Cr, Mn, Co, and Ni}$ for $x=0.17$ calculated in the LSDA.

imately 0.8 eV in lithium nitridomanganese in comparison with LiFeN . The narrow spin down peak of e_{2g} states which was pinned to E_F in LiFeN , is shifted upward by 0.8 eV in LiMnN . There is an energy gap between majority and minority states of around 0.47 eV. The spin magnetic moment (M_s) in Mn ($3.591 \mu_B$) is largest among other lithium nitridometalates, however, the M_l of Mn is extremely small because of Hund's second rule due to nearly half-filled bands. As a result, the MAE is also very small in LiMnN (lower panel of Fig. 8).

For the expected Co $3d^7$ configuration the majority spin electrons in LiCoN occupy five orbital states and minority spin electrons occupy two orbital states. Therefore the a_{1g} ($d_{zx}^\downarrow, d_{yz}^\downarrow$) bands are empty and lie 0.8–1.0 eV above E_F , while e_{2g} (d_{xy}^\downarrow and $d_{x^2-y^2}^\downarrow$) orbitals are completely occupied. Due to the spin splitting of the e_{1g} states the energy gap appears at the E_F of 0.646 eV. Similar to the LiFeN case, the width of e_{2g} bands in the LiCoN is extremely small due to weak direct Fe-Fe hybridization and comparable with the SO interaction strength. Figure 12 presents the energy band structure of LiCoN for $x=0.17$ for a non-relativistic (a), fully relativistic with $\mathbf{M} \parallel c$ axes (b), fully relativistic with $\mathbf{M} \perp c$ axes (c) and fully relativistic with orbital polariza-

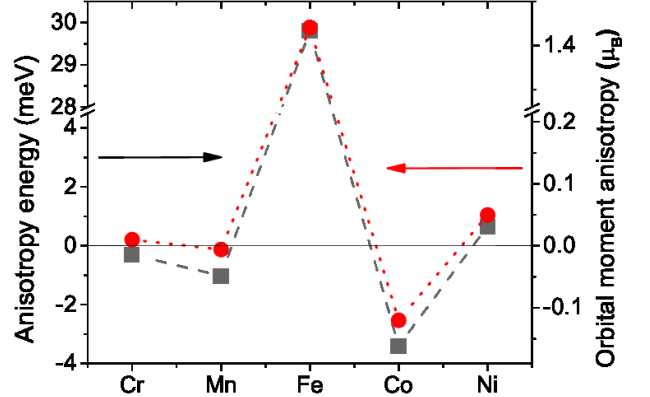


FIG. 9: (Color online) The MAE and OMA in LiMnN $M = \text{Cr, Mn, Fe, Co, and Ni}$ for $x=0.17$ calculated in the LSDA. Unusual fluctuations of the direction of easy magnetization axes coincide with sign changing OMA trend in accord with the second order PT and a Hund's rule.

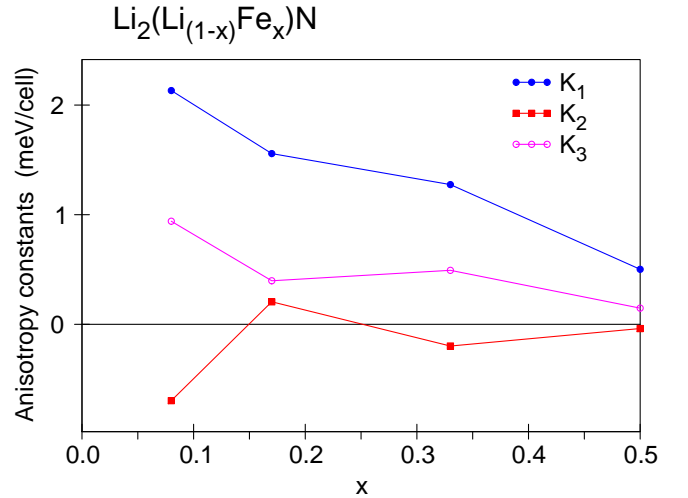


FIG. 10: (Color online) The anisotropy constants K_i for LiFeN as a function of the Fe concentration x .

tion (OP) correction (d). When $\mathbf{M} \parallel c$ the e_{2g} states are split by the SO interaction and form states with $m = -2$ and $m = +2$ (Fig. 12, lower panel). However, both states are occupied and the $m = \pm 2$ contributions to the Co M_l cancel each other to give a quite small OP in LiCoN . The M_l is $0.130 \mu_B$ for $\mathbf{M} \parallel c$. When $\mathbf{M} \perp c$ the M_l becomes very small ($M_l^\perp = 0.023 \mu_B$). The MAE reaches significant 3.5 meV/cell in LiCoN for $x=0.17$ with the easy axes in the ab plane.

LiNiN qualitatively has the same behavior of the MAE and orbital moments as a function of the magnetization direction as LiFeN . Both compounds have an easy

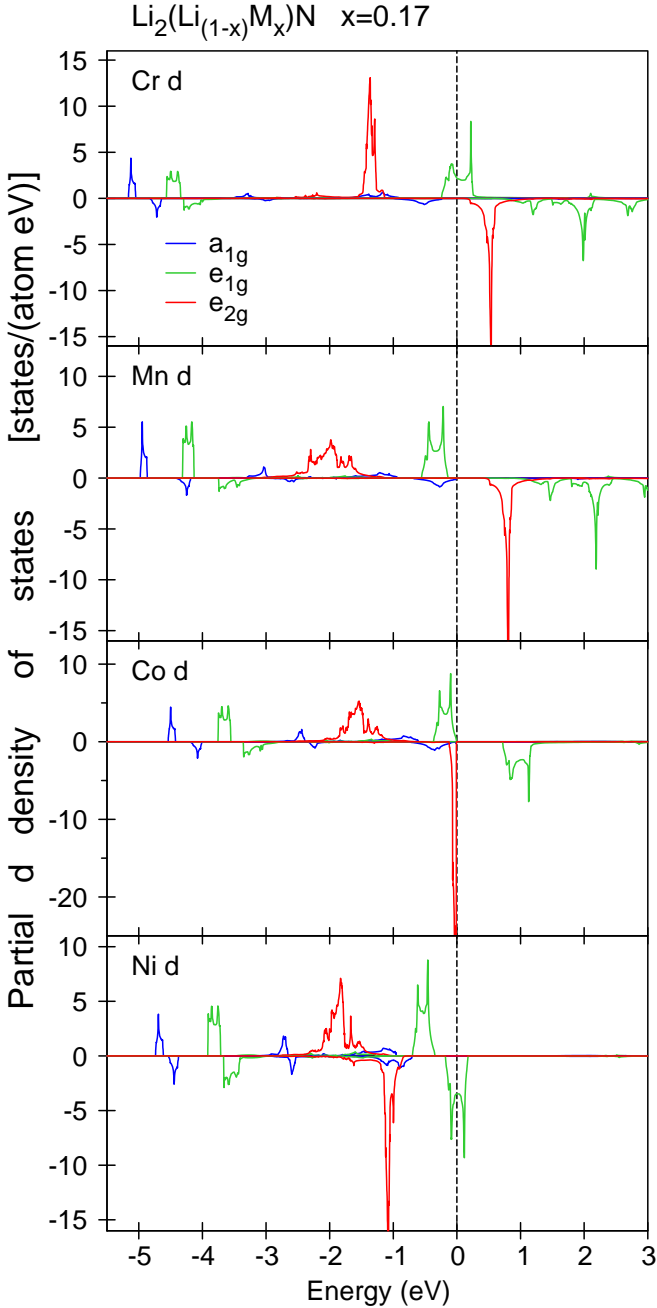


FIG. 11: (Color online) The LSDA transition metal 3d partial densities of states in lithium nitridometalates $\text{Li}_2(\text{Li}_{1-x}\text{M}_x)\text{N}$ ($\text{M} = \text{Cr}, \text{Mn}, \text{Fe}, \text{Co}, \text{and Ni}$) for $x=0.17$.

magnetization direction along the c axis and an almost quenched M_l in the ab plane. However, the M_l in LiNiN is one order of magnitude smaller and the MAE is significantly smaller compared to LiFeN (but still quite large from a point of view of permanent magnetism requirements). For the expected $\text{Ni } 3d^8$ configuration the majority spin electrons in LiNiN occupy five orbital states and minority spin electrons occupy three orbital states.

Therefore e_{2g} (d_{xy}^\downarrow and $d_{x^2-y^2}^\downarrow$) orbitals are completely occupied and e_{1g} (d_{zx}^\downarrow and d_{yz}^\downarrow) orbitals are filled by one electron in LiNiN (Fig. 11, lower panel). The width of e_{1g} bands is significantly larger than the width of the e_{2g} bands. Figure 13 presents the band structure of LiNiN for $x=0.17$ using a non-relativistic approximation, as well as fully relativistic with $\mathbf{M} \parallel c$ and $\mathbf{M} \perp c$ plane. When $\mathbf{M} \parallel c$, the diagonal $\hat{\mathbf{s}}\hat{\mathbf{l}}$ term couples d_{xz} and d_{yz} (see Table I) so the e_{1g} states are split due to the SO interaction and form states with $m = -1$ and $m=+1$. Because of the relatively large band width of the e_{1g} states the band formed by the $m = -1$ and the $m=+1$ states both are partly empty and partly occupied (Fig. 13 (b)). This results in a relatively small value of the $M_l=0.130 \mu_B$. When $\mathbf{M} \perp c$, in the local frame with $z' \parallel \mathbf{M}$ the d_{xz} and d_{yz} orbitals are transformed into other orbitals (e.g. $d_{xz} \rightarrow -d_{xz}$, $d_{yz} \rightarrow d_{xy}$, see Eqs. 2). The diagonal SO matrix elements between the d_{xz} and d_{xy} are equal to zero (Table I) and the bands positions are not affected by relativistic effects (compare non-relativistic bands in Fig. 13 (a) with fully relativistic with $\mathbf{M} \perp c$ in Fig. 13 (c)). The M_l becomes small ($M_l^\perp = 0.079 \mu_B$) while the total energy increases as compared to $E_{M \parallel c}$.

We conclude that only the LiFeN compound with a small concentration of Fe ions possesses a strong OMA and a huge MAE due to its unique energy band structure. Due to the SO interaction an extremely narrow energy band of a_{2g} symmetry (d_{xy}^\downarrow and $d_{x^2-y^2}^\downarrow$) is split to the states with $m=+2$ and -2 . Because of the small band width of the e_{2g} states, the band formed by the $m = -2$ state is completely filled and the $m=+2$ band is completely empty and the value of M_l is large. When $\mathbf{M} \perp c$ the diagonal SO matrix elements between these orbitals became equal to zero, the energy bands are not split by the SO interaction and the M_l becomes zero. The SO coupling in LiFeN leads to an appearance of a nearly insulating state solely due to the SO coupling (see Fig. 5).

We also investigate the electronic structure of LiMn ($\text{M} = \text{Cu}, \text{Ru}, \text{and Os}$). However, the ferromagnetic solution for these compounds is not stable.

B. Optical and magneto-optical properties.

Figure 14 presents calculated optical conductivity $\sigma(\omega)$, real part $\varepsilon_{1xx}(\omega)$ and imaginary part $\varepsilon_{2xx}(\omega)$ of the dielectric function and optical reflectivity $R(\omega)$ in LiFeN using the LSDA+OP. As we discussed, the SO splitting for two magnetization \mathbf{M} directions is different: for $\mathbf{M} \parallel c$ the energy bands have SO splitting at E_F while for $\mathbf{M} \perp c$ this splitting is absent. As a result, we have a different behavior of the diagonal optical functions (Fig. 14). However, the absolute values of the optical functions for different magnetization directions are similar.

The situation is remarkably different for the non-diagonal matrix elements. Fig. 15 presents the Kerr ro-

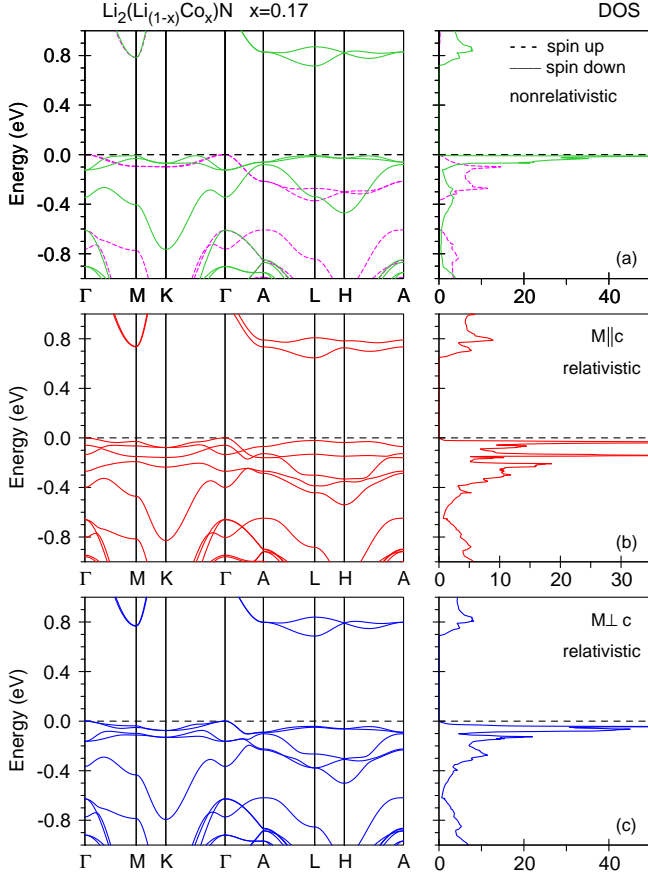


FIG. 12: (Color online) Energy band structure and DOS [in states/(cell eV)] of LiCoN for $x=0.17$: a non-relativistic (a), fully relativistic with $\mathbf{M} \parallel c$ (b), and $\mathbf{M} \perp c$ (c).

tation (θ_K) and the Kerr ellipticity (ε_K) calculated in the LSDA+OP. The off-diagonal optical conductivity, σ_{1sxx} and σ_{2sxy} is shown in Fig. 16. We found a very large Kerr rotation in LiFeN presented as a number of separated peaks with a similar amplitude of about -2° at 1.5 to 5.5 eV for $\mathbf{M} \parallel c$. On the other hand, for $\mathbf{M} \perp c$ the Kerr rotation and Kerr ellipticity simply vanish.

An important issue is to identify the origin of the large Kerr effect in LiFeN. To this end, we examine the dependence of the MO spectra on the exchange splitting and the SO interaction. The exchange splitting and the SO coupling are studied by scaling the corresponding terms in the Hamiltonian. We found that with zero exchange splitting on Li and N ($\Delta_{Li,N}=0$, dotted black curve in lower panel of Fig. 15), the Kerr rotation remains the same. But when the exchange splitting on Fe is absent ($\Delta_{Fe}=0$, dashed magenta curve in lower panel of Fig. 15), the Kerr rotation almost disappears. With no SO coupling on Li or N, the Kerr rotation is the same as before ($\lambda_{Li,N}=0$, dashed red curve in lower panel of Fig. 15). On the other hand, when the SO coupling on Fe is zero ($\lambda_{Fe}=0$, full green curve in lower panel of Fig. 15), the Kerr rotation totally vanishes. Thus, the SO coupling

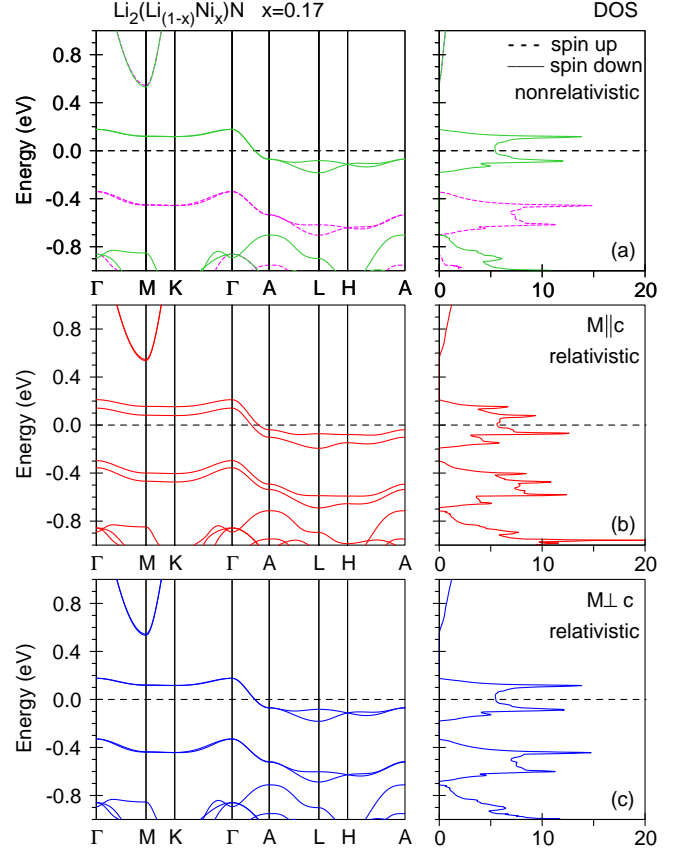


FIG. 13: (Color online) Energy band structure and DOS [in states/(cell eV)] of LiNiN for $x=0.17$: a non-relativistic (a), fully relativistic with $\mathbf{M} \parallel c$ (b), and with $\mathbf{M} \perp c$ axes (c).

and the exchange splitting of Fe are equally responsible for the large Kerr rotation in LiFeN. From these investigations, the following picture of the Kerr effect in LiFeN emerges: Fe is the only magneto-optically active element which is solely responsible for the large Kerr rotation effects in this system.

As we mentioned above, Fe 3d states are weakly hybridized with the N and Li p states. It is clearly seen in Fig. 17 where we present the energy band structure of LiFeN in a so-called "fat band" representation. Red circles show the Fe 3d character of the wave function in each \mathbf{k} point. The larger circle corresponds to the larger contribution of the corresponding character in the wave function for a given \mathbf{k} point. Fe 3d energy bands around -2 eV below the E_F at the $M-K$ symmetry direction show a small hybridization with N 2p states. However, other energy bands with predominant Fe 3d character show a very small hybridization with the N and Li p states and possess an almost atomic character in LiFeN ($x \leq 0.17$).

If the diagonal optical conductivity σ_{1sxx} appears as the interband optical transitions between occupied and empty energy bands which are formed by all the elements in the compound, then the off-diagonal conductivity (Fig.

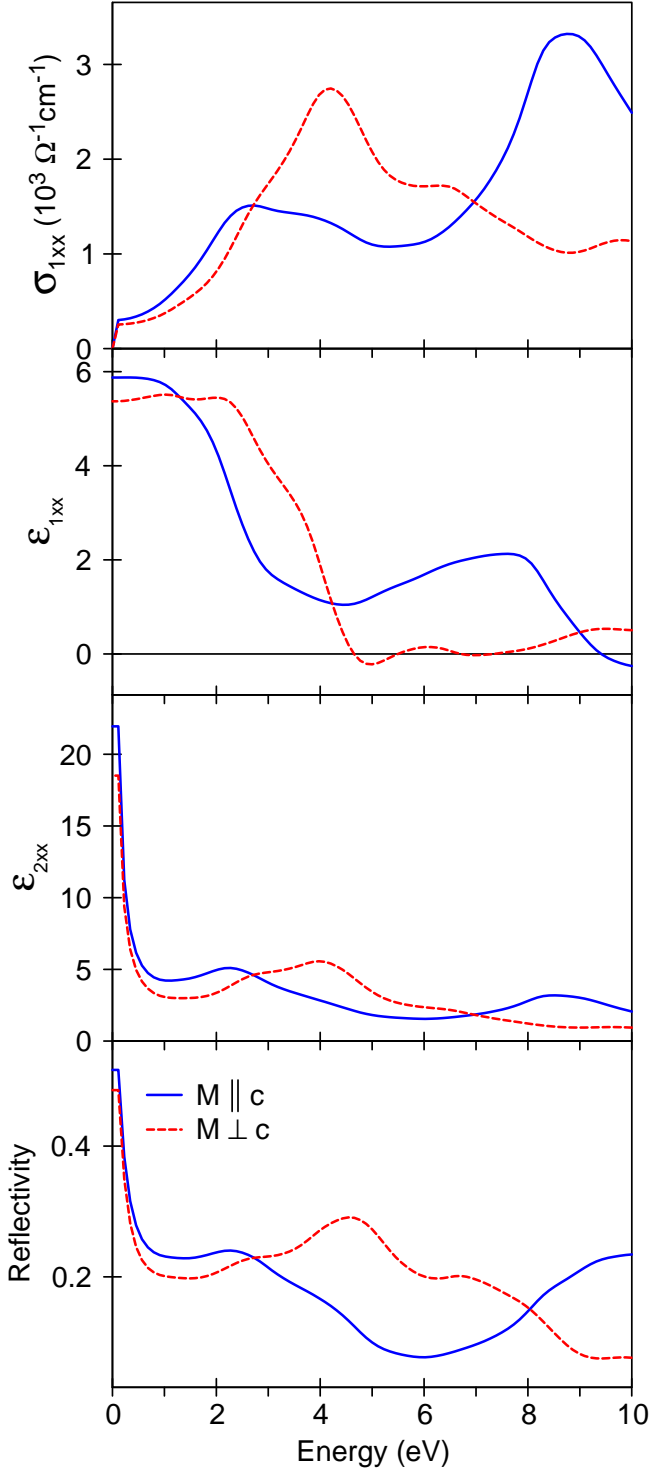


FIG. 14: (Color online) Calculated in the LSDA+OP approximation the optical conductivity $\sigma(\omega)$, real part $\epsilon_{1xx}(\omega)$ and imaginary part $\epsilon_{2xx}(\omega)$ of the dielectric function and optical reflectivity $R(\omega)$ of LiFeN for with $\mathbf{M} \parallel c$ (full blue curves) and $\mathbf{M} \perp c$ (dashed red curves).

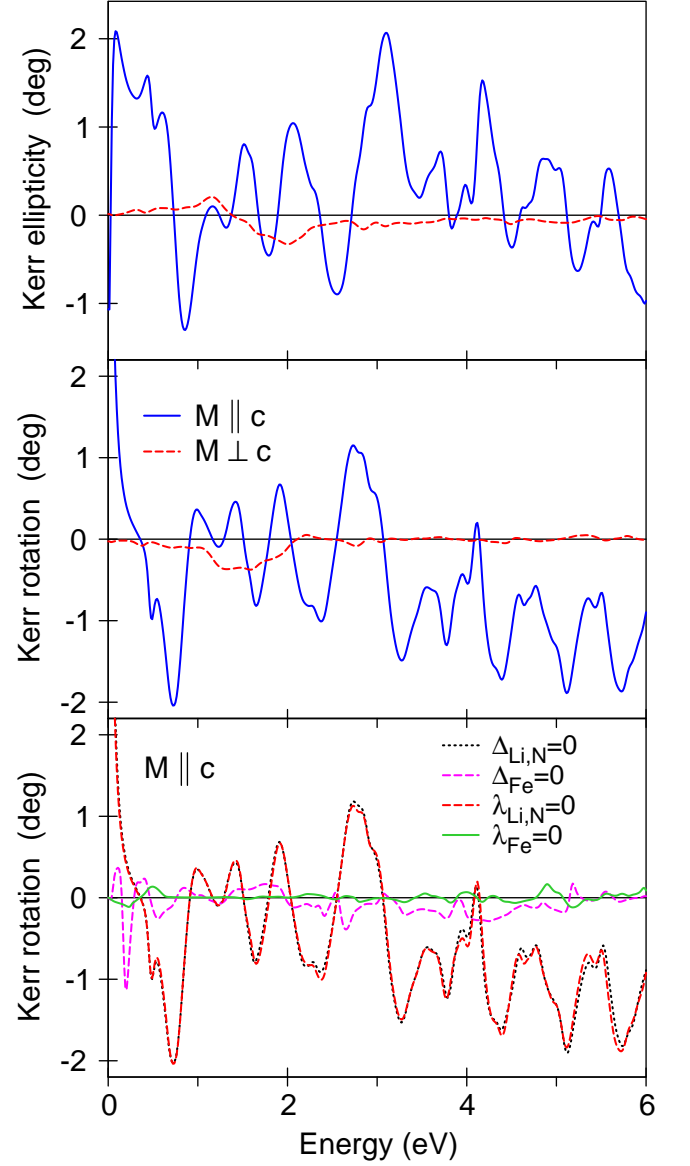


FIG. 15: (Color online) Calculated in the LSDA+OP approximation polar Kerr ellipticity ϵ_K (upper panel) and Kerr rotation θ_K (middle panel) spectra of LiFeN with $\mathbf{M} \parallel c$ (full blue curves) and with $\mathbf{M} \perp c$ (dashed red curves). Lower panel shows the influence of the exchange splitting (Δ) and SO coupling (λ) on the Kerr rotation of LiFeN for $\mathbf{M} \parallel c$ (see the text).

16) as well as Kerr spectra (Fig. 15) are formed by the interband transitions mostly between occupied and empty Fe 3d energy bands. Also, Fe 3d bands possess an almost atomic character due to small hybridization with other states. As a result, the MO Kerr rotation spectrum is consisted of a quasi atomic-like spectrum with number separated peaks with similar amplitude.

We also calculated the MO Kerr spectra using the LSDA+ U for different Hubbard $U = 2, 3,$ and 4 eV. Preliminary results for $U = 4$ eV have been published

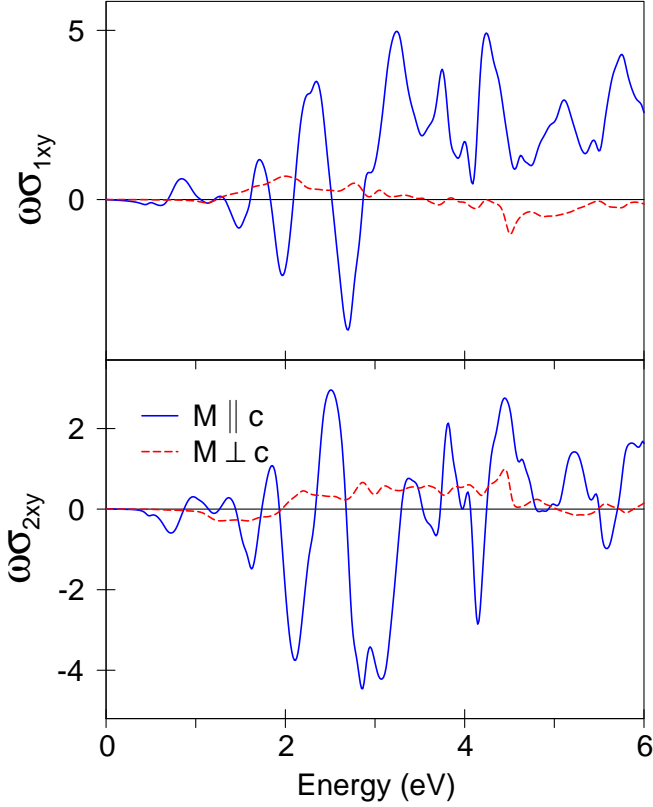


FIG. 16: (Color online) Calculated in the LSDA+OP off-diagonal component σ_{1xy} and σ_{2xy} (in 10^{29} s^{-2}) of the conductivity tensors of LiFeN with $\mathbf{M} \parallel c$ (full blue curves) and with $\mathbf{M} \perp c$ (dashed red curves).

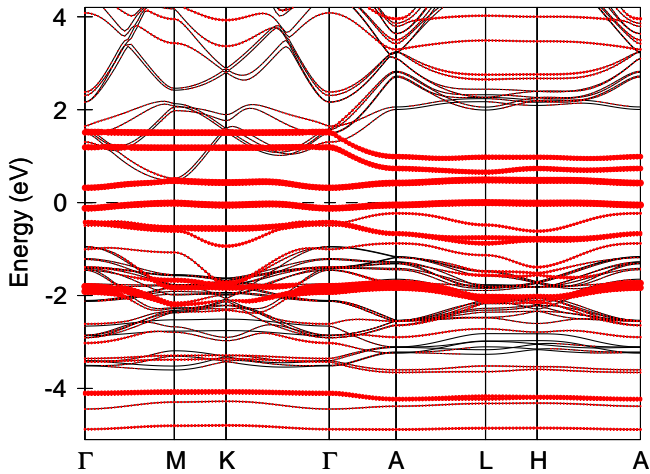


FIG. 17: (Color online) The energy band structure of LiFeN in "fat band" representation. Red circles show the Fe $3d$ character of the wave function in each \mathbf{k} point.

elsewhere.⁵⁷ The resulting spectra are similar to the LSDA and LSDA+OP ones with different energy position of quasi atomic-like peaks. Besides, with increasing Hubbard U the intensity of the peaks is increased reaching -4° at around 4.8 eV for $U = 4$ eV.⁵⁷ The experimental investigation of the Kerr spectra in LiFeN is highly desirable. Due to high sensitivity of the intensity and energy position of quasi atomic peaks of Kerr spectra to the value of U , the comparison between the theoretically calculated and experimentally measured spectra might be an excellent opportunity to estimate a value of the Hubbard U in LiFeN.

Unusually high anisotropy of Kerr angle and conductivity in general is not surprising because the obtained above the large OMA. For instance, the relation between M_l and $\sigma_{xy}^{(2)}(\omega)$ has been discussed in Ref. 58,59. So we can safely assume that OMA is proportional to the following sum rule for the anisotropy of the off-diagonal optical conductivity tensor

$$\Delta M_l \sim \int d\omega \Delta \sigma_{2xy}(\omega) \quad (21)$$

This expression is non-trivial as its left part contains only spin longitudinal components (see definition in Eq. 13) while the off-diagonal conductivity tensor contains contributions from both spin longitudinal and transversal matrix elements of the SO coupling. Thus we found that the OMA is a key quantity which determines a behavior of many important magneto anisotropic properties (both static and dynamic) of the magnetic systems. We will study this and related dependencies in our forthcoming papers.

C. X-ray magnetic circular dichroism.

The X-ray absorption and XMCD spectra in metals at the K edge in which the $1s$ core electrons are excited to the p states through the dipole transition usually attract only minor interest, because p states are not the states of influencing magnetic or orbital order. Recently, however, understanding p states has become important since XMCD spectroscopy using K edges of transition metals became popular. The K edge XMCD is sensitive to electronic structures at neighboring sites due to the delocalized nature of the p states. Fig. 18(upper panel) shows the theoretically calculated X-ray absorption spectra at the Fe K edge in LiFeN with $\mathbf{M} \parallel c$ (blue full curve) and $\mathbf{M} \perp c$ axes (red dashed curve) in comparison with the experimental measurements by Yamada *et al.*¹⁰ The XAS spectra for both the magnetization directions are very similar in both shape and amplitude.

Figure 18(lower panel) shows the theoretically calculated XMCD in terms of the difference in absorption $\Delta\mu_K = \mu_K^+ - \mu_K^-$ for left and right circularly polarized radiation at the Fe K edge in LiFeN. The exchange splitting of the initial $1s$ -core state is extremely small, therefore

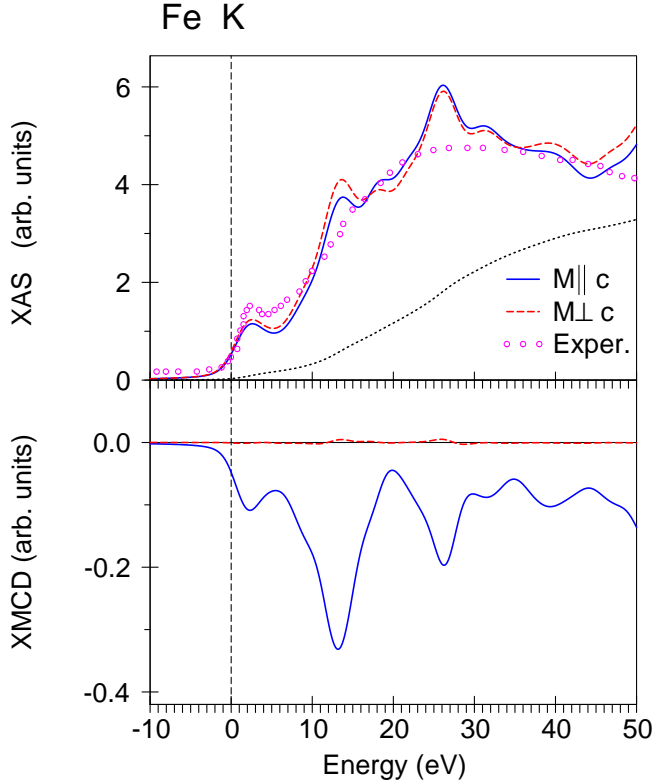


FIG. 18: (Color online) upper panel: the measured XAS¹⁰ of LiFeN at the Fe K edge for $x=0.32$ and the calculated one for $x=0.33$ with $\mathbf{M} \parallel c$ (blue full curve) and $\mathbf{M} \perp c$ (red dashed curve), black dotted curve shows the background scattering intensity; lower panel: the calculated XMCD spectrum at the Fe K edge with $\mathbf{M} \parallel c$ (blue full curve) and $\mathbf{M} \perp c$ (red dashed curve).

only the exchange and SO splitting of the final $4p$ -states is responsible for the observed dichroism at the K -edge. The XMCD spectrum for the $\mathbf{M} \parallel c$ is relatively large and extended up to 50 eV (full blue curve in lower panel of Fig. 18). However, the XMCD spectrum for the $\mathbf{M} \perp c$ is completely vanished due to smallness of the SO interaction for this magnetization direction.

Figure 19 shows the calculated Fe $L_{2,3}$ XMCD spectra in LiFeN. In contrast to the K -edge, where there is a large difference in the XMCD spectra for the $\mathbf{M} \parallel c$ and $\mathbf{M} \perp c$ polarizations, the XMCD at the $L_{2,3}$ edges only slightly differ from each other for the two magnetic polarization directions. The dichroism at the L_2 - and L_3 -edges is also influenced by the SO coupling and exchange splitting of the initial $2p$ -core states. This gives rise to a very pronounced dichroism in comparison with the dichroism at the K edge. The SO splitting of the initial Fe $2p$ -core state in LiFeN is equal to 12.4 eV, which is much larger than the SO splitting of the final band states of around 0.1 eV. Therefore, the quenched SO interaction in valent states for the $\mathbf{M} \perp c$ polarization only slightly reduces the dichroism at the $L_{2,3}$ edges in comparison with the

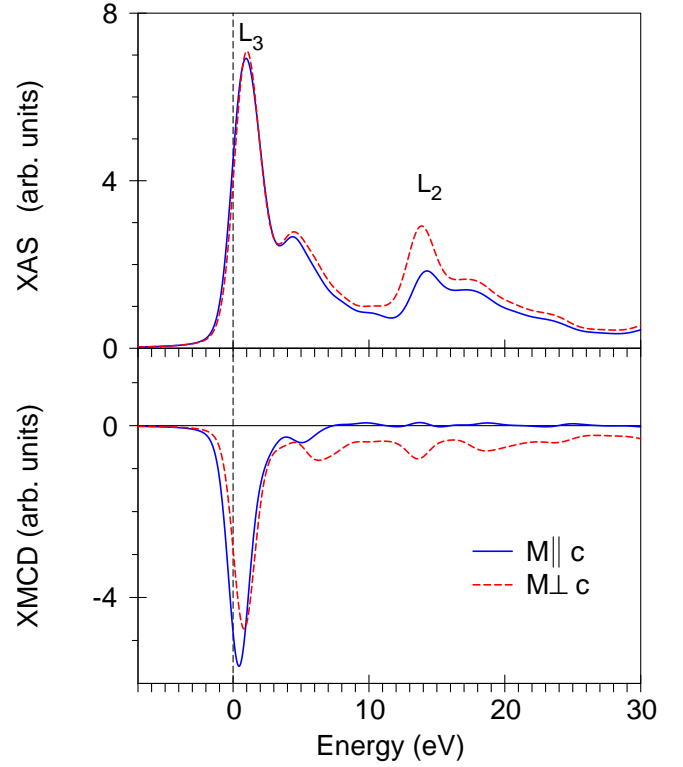


FIG. 19: (Color online) upper panel: the calculated x-ray absorption spectra of LiFeN at the Fe $L_{2,3}$ edges for $x=0.33$ with $\mathbf{M} \parallel c$ (blue full curve) and $\mathbf{M} \perp c$ (red dashed curve); lower panel: the calculated XMCD spectrum at the Fe $L_{2,3}$ edges with $\mathbf{M} \parallel c$ (blue full curve) and $\mathbf{M} \perp c$ (red dashed curve).

$\mathbf{M} \parallel c$ polarization (Fig. 19).

A further investigation of the XAS and XMCD spectra in LiFeN at the K and $L_{2,3}$ edges is highly recommended.

IV. CONCLUSIONS.

The electronic structure and physical properties of lithium nitridometalates $\text{Li}_2(\text{Li}_{1-x}\text{M}_x)\text{N}$ ($\text{M} = \text{Cr}, \text{Mn}, \text{Fe}, \text{Co}, \text{and Ni}$) were theoretically investigated from the first principles. We found that only the LiFeN compound with a small concentration of Fe ions possesses a huge OMA and MAE due to its unique energy band structure. This compound has an extremely narrow energy band of a_{2g} symmetry (d_{xy}^\downarrow and $d_{x^2-y^2}^\downarrow$) of spin down at the Fermi level forming a half-metallic state. When $\mathbf{M} \parallel c$, the diagonal SO l_z operator couples d_{xy} and $d_{x^2-y^2}$ so that they form states with $m = -2$ and $+2$. Because of the small band width of the e_{2g} states the band formed by the $m = -2$ state is completely filled and the $m = +2$ band is empty. This gives a large value of the M_l which is almost completely unquenched. When $\mathbf{M} \perp c$ the diagonal SO matrix elements between these orbitals

became equal to zero, the energy bands are not affected by the SO coupling the M_l almost disappears. Thus, the large OMA and MAE is observed. It can be concluded that the SO coupling energy contributes to the total energy only when $\mathbf{M} \parallel c$, while in-plane it is practically absent. Therefore, the SO coupling energy practically coincides with the anisotropy energy, creating a system with a maximum of MAE.

We found that LiFeN presents quite a rare example of the single-ion anisotropy $3d$ electron compound where due to strong localization of the $3d$ orbitals the pair Neel type anisotropy is very small.

LiMnN and LiCoN were found to be insulators with quite a large energy gap of 0.50 and 0.58 eV, respectively. The spin magnetic moment at the Mn site in LiMnN ($3.591 \mu_B$) is largest among other lithium nitridometalates. However, the orbital magnetic moment of Mn is small due to a nearly half-filled band. As a result, the MAE strongly reduces its absolute value and changes its sign in both LiMnN and LiCoN.

A very non-trivial strongly fluctuating and sign changing character of the magnetic anisotropy with electronic doping is predicted theoretically. Specifically for Cr and Mn systems the easy magnetization axes is in plane, while for Fe system it is along z-direction (with enormous amplitude of MAE). Co system has already relatively large in-plane anisotropy, while Ni system demonstrates a small uniaxial anisotropy. This unusual dependence is supported by corresponding orbital moment anisotropy.

The Kerr ellipticity and rotation spectra are formed by interband transitions mostly between magneto-optical active atomic-like Fe $3d$ bands. As a result, the Kerr spectra consist of a number of separated peaks with similar amplitude in the energy interval between 1.5 and 5.5 eV. Thus, we predict that MO experiments should demonstrate the nearly atomic structure of energy levels in this system. The anisotropy of the Kerr angle and corresponding off-diagonal conductivity have been obtained for LiFeN. It looks like this anisotropy is also related to the orbital moment anisotropy.

We have studied the XAS and XMCD spectra of LiMn at the Fe K , and $L_{2,3}$ edges. A very strong anisotropy of the X-ray magnetic dichroism for the K spectrum was found.

Only the exchange and the SO splitting of the final $4p$ -states are responsible for the observed dichroism at the K -edge. Due to the quenching of the SO interaction for the $\mathbf{M} \perp c$ the Fe K XMCD spectrum is completely vanished for this magnetization direction. However, the dichroism at the $L_{2,3}$ edges is also influenced by the SO coupling and exchange splitting of the initial $2p$ -core states. The SO splitting of the initial Fe $2p$ -core state in LiFeN is much larger than the SO splitting of the final band states. Therefore, the quenched SO interaction in valent states for the $\mathbf{M} \perp c$ polarization only slightly reduces the dichroism at the $L_{2,3}$ edges in comparison with the $\mathbf{M} \parallel c$ polarization.

From a point of view of possible applications, it is highly desirable to increase the Curie temperature of these systems without losing high magnetic anisotropy. A possible nanocomposite of LiFeN and a soft phase with a large Curie temperature (like FeCo) seems promising.

Acknowledgments

This research is supported by the Critical Materials Institute, an Energy Innovation Hub funded by the U.S. DOE, Office of Energy Efficiency and Renewable Energy, Advanced Manufacturing Office; and the U.S. DOE Office of Basic Energy Science, Division of Materials Science and Engineering. Ames Laboratory is operated for the U.S. DOE by Iowa State University under contract DE-AC02-07CH11358. We are thankful to A.N. Yaresko for helpful discussions and providing us the matrix elements of the SO interaction. V.P.A. is thankful to A.V. Antropov for useful comments. V.N.A. gratefully acknowledges the hospitality at Ames National Laboratory during his stay there.

¹ M. Nishijima, T. Kagohashi, Y. Takeda, M. Imanishi, and O. Yamamoto, *J. Power Sources* **68**, 510 (1997).

² T. Shodai, Y. Sakurai, and T. Suzuki, *Solid State Ionics* **122**, 85 (1999).

³ Y. Takeda, M. Nishijima, M. Yamahata, K. Takeda, N. Imanishi, and O. Yamamoto, *Solid State Ionics* **130**, 61 (2000).

⁴ A. Rabenau, *Solid State Ionics* **6**, 277 (1982).

⁵ M. Nishijima, T. Kagohashi, M. Imanishi, Y. Takeda, O. Yamamoto, and S. Kondo, *Solid State Ionics* **83**, 107 (1996).

⁶ T. Shodai, S. Okada, S. Tobishima, and J. Yamaki, *Solid State Ionics* **86–88**, 785 (1996).

⁷ P. Chen, Z. Xiong, J. Luo, J. Lin, and K. L. Tan, *Nature* **420**, 302 (2002).

⁸ Y. Nakamori, G. Kitahara, K. Miwa, S. Towata, and

S. Orimo, *Appl. Phys. A: Mater. Sci. Process.* **80**, 1 (2005).

⁹ J. Zhang, R. Cerny, B. Villeroy, C. Godart, D. Chandra, and M. Latroche, *J. Appl. Crystallogr.* **509S**, S732 (2011).

¹⁰ A. Yamada, S. Matsumoto, and Y. Nakamura, *J. Mater. Chem.* **21**, 10021 (2011).

¹¹ R. Juza, K. Langer, and K. V. Benda, *Angew. Chem., Int. Ed. Engl.* **7**, 321 (1968).

¹² R. Niewa, D. Zhrebtsov, and Z. Hu, *Inorg. Chem.* **42**, 2479 (2003).

¹³ W. Sachsze and R. Juza, *Z. Anorg. Allg. Chem.* **259**, 278 (1949).

¹⁴ J. Klatyk and R. Kniep, *Z. Kristallogr. NCS* **214**, 447 (1999).

¹⁵ R. Niewa, F. R. Wagner, W. Schnelle, O. Hochrein, and R. Kniep, *Inorg. Chem.* **40**, 5215 (2001).

¹⁶ G. Kerker, *Phys. Rev. B* **23**, 6312 (1978).

- ¹⁷ P. Blaha, J. Redinger, and K. Schwarz, *Z. Physik B* **57**, 273 (1984).
- ¹⁸ R. Dovesi, C. Pisani, F. Ricca, C. Roetti, and V. R. Saunders, *Phys. Rev. B* **30**, 972 (1984).
- ¹⁹ J. Klatyk, W. Schnelle, F. R. Wagner, R. Niewa, P. Novák, R. Kniep, M. Waldeck, V. Ksenofontov, and P. Gülich, *Phys. Rev. Lett.* **88**, 207202 (2002).
- ²⁰ P. Novák and F. R. Wagner, *Phys. Rev. B* **66**, 184434 (2002).
- ²¹ P. Novák and F. R. Wagner, *J. Magn. Magn. Mater.* **272–276**, e269 (2004).
- ²² Y. Yan, J. Y. Zhang, T. Cui, Y. Li, Y. M. Ma, J. Gong, Z. G. Zong, and G. T. Zou, *Eur. Phys. J. B* **61**, 397 (2008).
- ²³ T. T. Fister, G. T. Seidler, E. L. Shirley, F. D. Vila, J. J. Rehr, K. P. Nagle, J. C. Linehan, and J. O. Cross, *J. Chem. Phys.* **129**, 044702 (2008).
- ²⁴ S. Wu, Z. Dong, F. Boey, and P. Wu, *Appl. Physics Lett.* **94**, 172104 (2009).
- ²⁵ A. Wu, Z. Dong, P. Wu, and F. Boey, *J. Mat. Chemistry* **21**, 165 (2011).
- ²⁶ W. Kress, H. Grimm, W. Press, and J. Lefebvre, *Phys. Rev. B* **22**, 4620 (1980).
- ²⁷ H. R. Chandrasekhar, G. Bhattacharya, R. Migoni, and H. Bilz, *Phys. Rev. B* **17**, 884 (1978).
- ²⁸ J. Sarnthein, K. Schwarz, and P. Blöchl, *Phys. Rev. B* **53**, 9084 (1996).
- ²⁹ Y. Zhao, X. Tian, W. Xue, and T. Gao, *Solid State Commun.* **149**, 2130 (2009).
- ³⁰ R. Kniep, *Pure Appl. Chem.* **69**, 185 (1997).
- ³¹ R. Niewa, Z. L. Huang, W. Schnelle, Z. Hu, and R. Kniep, *Z. Anorg. Allg. Chem.* **629**, 1778 (2003).
- ³² W. Schnelle, R. Niewa, and F. Wagner, *J. Magn. Magn. Mater.* **272–276**, 828 (2004).
- ³³ V. Ksenofontov, S. Reiman, M. Waldeck, R. Niewa, R. Kniep, and P. Gülich, *Z. Anorg. Allg. Chem.* **629**, 1787 (2003).
- ³⁴ A. Jesche, R. W. McCallum, S. Thimmaiah, J. L. Jacobs, V. Taufour, A. Kreyssig, R. S. Houk, S. L. Bud'ko, and P. C. Canfield, *Nature Commun.* **5**, 3333 (2014).
- ³⁵ J. Smit and H. P. J. Wijn, *Ferrites* (Philips Technical Library, Eindhoven, 1959).
- ³⁶ A. Abragam and B. Bleaney, in *Electron Paramagnetic Resonance of Transition Ions* (Oxford University Press, Oxford, 1970), p. 911.
- ³⁷ K. Yosida, A. Okiji, and S. Chikazumi, *Prog. Theor. Phys.* **33**, 559 (1965).
- ³⁸ R. L. Streever, *Phys. Rev. B* **19**, 2704 (1979).
- ³⁹ V. P. Antropov, *PhD Thesis* (Institute of Physics of Metals, Sverdlovsk, Russia (in Russian), 1986).
- ⁴⁰ H. Ebert, R. Zeller, B. Drittler, and P. Dederichs, *J. Appl. Phys.* **67**, 4576 (1990).
- ⁴¹ I. V. Solovyev, P. H. Dederichs, and I. Mertig, *Phys. Rev. B* **52**, 13419 (1995).
- ⁴² V. P. Antropov, L. Ke, and D. Aberg, *Solid State Commun.* **194**, 35 (2014).
- ⁴³ M. Cinal, D. M. Edwards, and J. Mathon, *Phys. Rev. B* **50**, 3754 (1994).
- ⁴⁴ G. van der Laan, *J. Phys.: Condens. Matter* **10**, 3239 (1998).
- ⁴⁵ J. Stöhr and H. Siegmann, in *Magnetism. From fundamentals to Nanoscale Dynamics* (Springer-Verlag, Berlin Heidelberg, 2006), p. 805.
- ⁴⁶ I. Hubac and S. Wilson, *J. Phys. B: At. Mol. Opt. Phys.* **33**, 365 (2000).
- ⁴⁷ A. V. Postnikov and V. P. Antropov, *Comp. Mat. Sci.* **17**, 438 (2000).
- ⁴⁸ E. Zintl and G. Bauer, *Z. Elektrochem.* **41**, 102 (1935).
- ⁴⁹ D. H. Gregory, P. M. O'Meara, A. G. Gordon, J. P. Hodges, S. Short, and J. D. Jorgensen, *Chem. Mater.* **14**, 2063 (2002).
- ⁵⁰ V. N. Antonov, A. Y. Perlov, A. P. Shpak, and A. N. Yaresko, *J. Magn. Magn. Mater.* **146**, 205 (1995).
- ⁵¹ O. K. Andersen, *Phys. Rev. B* **12**, 3060 (1975).
- ⁵² P. E. Blöchl, O. Jepsen, and O. K. Andersen, *Phys. Rev. B* **49**, 16223 (1994).
- ⁵³ A. N. Yaresko, V. N. Antonov, and P. Fulde, *Phys. Rev. B* **67**, 155103 (2003).
- ⁵⁴ M. T. Czyżyk and G. A. Sawatzky, *Phys. Rev. B* **49**, 14211 (1994).
- ⁵⁵ A. I. Liechtenstein, V. I. Anisimov, and J. Zaanen, *Phys. Rev. B* **52**, R5467 (1995).
- ⁵⁶ O. Eriksson, B. Johansson, and M. S. S. Brooks, *J. Phys.: Condens. Matter* **1**, 5005 (1989).
- ⁵⁷ V. Antonov, L. Ke, A. Jesche, and V. Antropov, *Bulletin of the American Physical Society, APS March Meeting 2013* **58**, F22.00008 (2013).
- ⁵⁸ D. Weller, G. R. Harp, R. F. C. Farrow, A. Cebollada, and J. Sticht, *Phys. Rev. Lett.* **72**, 2097 (1994).
- ⁵⁹ P. M. Oppeneer, *J. Magn. Magn. Mater.* **188**, 275 (1998).